

POLITECNICO DI TORINO

NANOTECHNOLOGY FOR ICT

Characterization of Suspended Micro Channel Resonators

Author:
Kofi Bempah OWUSU

Supervisor:
Prof. Ricciardi CARLO
Dr. Stefano STASSI
Dr. Roberta CALMO



Abstract

The Suspended Microchannel Resonators (SMRs) are recently attracting great attention in the biosensing field, and in particular in the density and mass monitoring of cells, bacteria growth and particles loading. One of the main drawback in the implementation of this platform in lab-on-chip devices is represented by the time consuming and expensive fabrication approach used to create the SMR itself. In fact, in order to realized a buried channel in a suspended structure complex fabrication methods are needed, which requires several photo lithographic, depositions and etching process. In this work it has proposed an innovative method of fabrication based on the femtosecond laser writing. In particular a glass SMR has been fabricated optimizing a two steps fabrication process, which includes the patterning of the buried channel and of the suspended beam followed by a chemical etching of the exposed substrates. The strength of this approach is represented by the possibility to define and release the buried channel just simply patterning the geometries with the laser that can be focused at any depth inside the silica glass. Furthermore, considering the simplicity of this method a new SMRs design was optimized. This is characterized by the presence of specific obstacles in the middle of the buried channel that in principles, could be used to reduce the liquid flow velocity. This means to have the possibility to increase the time of permanence of cells, bacteria and particles in the beam region, which gives the higher amplitude signal. In this perspective, the main purpose of this thesis work was to understand how the mechanical behavior of SMRs could be affected by the presence of this constriction geometries build inside the hollow channel. In order to do that some fundamental aspect should be take into account: first the simulation of the mechanical behavior of the SMRs with the constriction; second, the experimental confirm of this behavior; and third the mechanical performance of the SMRs containing the constriction have to be compared with SMRs characterized by the same dimensions but without constriction. Furthermore, the effective ability of the new SMR design in distinguish liquid with different density must be verify. Remarkable correlation exist between the characterized resonance frequencies that were obtained from the experimental measurement and the values obtained from modeling the suspended microchannel resonators using Comsol. In fact, the variation percentage of these values is less than 4%. In total four suspended microchannel resonators were model and characterized in this study, characterized by four different constriction geometries. The four suspended micro channel resonators were model using the Multiphysics Comsol applying the solid mechanics suite. The first flexural eigenfrequencies for the four resonators were theoretical computed to be 1.0334 MHz, 1.0336 MHz, 1.0905 MHz and 0.4938 MHz respectively. The model did not only provide the first flexural mode but also model generated the second, third flexural mode as well as the first torsional mode for each suspended micro channel resonator. The final stage of the simulation was to perform the above simulation filling the micro channel with liquids and theoretical computing the eigenfrequency. From the experimental point of view, a mechanical characterization was performed by the means of a Laser Doppler Vibrometer. The main properties of the SMRs were extracted from this measurements and Q factor, Responsivity and Frequency stability have been defined for each SMRs. The presence of the constriction in the middle of the buried channel seems does not affect in a negative way the Responsivity and the Frequency stability of the SMRs. On the contrary, the Q factor shows a worsening for the SMRs containing the constriction respect to the SMRs without it. Finally, in order to evaluate the effective capability of the SMRs (fabricated with the new design) three different liquids were made to flow through the suspended micro channel resonator and the experimental sensitivity with the minimum detectable mass were computed. The experimental results are in agreement with what was observed from the simulation, and the minimum detectable mass obtained (in the range of hundreds of femtograms) reveal that this platforms can be competitive with the well know SMRs already presented in the literature.

Dedication

This work is dedicated to the almighty God, my immediate families and EDISU who through their financial help have brought me thus far in my education. I am also highly grateful to my supervisors, Roberta and all our lecturers who diligently taught me the value of knowledge.

Declaration

I hereby declare that I have undertaken the project herein under the supervision of Prof. Carlo Ricciardi. and Dr. Stassi Stefano.

Names:

SIGNATURE:

.....
OWUSU BEMPAH KOFI

DATE:.....

I declare that I supervised the student who have undertaken the project and I can confirm that he have my permission to present it for assessment.

Names:

SIGNATURE:

.....
CARLO RICCIARDI
(Lecturer,Politecnico Di Torino)

DATE:.....

Acknowledgements

I thank the almighty God for helping me to successfully complete this thesis by granting me life, wisdom and understanding. Indeed God have lead me all the way through my trauma and depression while perusing my master degree in nanotechnology at politecnico di torino. I give the almighty God all the praise.

I also extend a big gratitude to my supervisors, Prof. Carlo Ricciardi, Dr. Calmo Roberta and Dr. Stassi Stefano who guided and advised me throughout this work. To my mother Sylvia Ross Effie Seguwah Thompson, I say a big thank you for all your prayers and financial support you have given me up to this time.

Contents

1	Introduction	13
1.1	Origin Of Microcantilever	13
1.2	Operating Modes	13
1.2.1	Static Mode	13
1.2.2	Dynamic Mode	14
1.3	Suspended Micro And Nano Resonator	15
1.4	Application Of SMR	16
1.5	Microfluidic Resonators Fabrications	18
2	Theory	21
2.1	Resonance Frequency	21
2.1.1	Eigenmodes of Ideal Continuum Mechanical Structures	21
2.2	Free Bending Vibrations Of Beams	23
2.3	Bridges	25
2.4	Lumped Element Resonator Models	27
2.4.1	Freely Damped Resonator	28
2.4.2	Driven Damped Resonator	29
2.5	Quality Factor	30
2.5.1	Quality Factor	30
2.5.2	Responsivity	31
2.5.3	Allan Variance	32
3	Device Fabrication	35
3.1	Femtosecond Laser Microstructuring	35
3.2	Fundamental Physical Mechanism Of Femtosecond Laser Microfluidic Fabrication	36
3.2.1	Non-Linear Mechanism	36
3.3	Non Linear Absorption Pulses	37
3.3.1	Modification classes based on laser fluence	37
3.4	Methods for femtosecond microfluidic writing	38
3.4.1	Femtosecond Writing Set Up	38
3.5	Fabricated Suspended Microchannel Resonator	39
3.6	Process Flow For PDMS Integration	40
3.6.1	Silicon Mold Process Flow	41
3.6.2	PDMS Glass Bonding Process Flow	42
4	Methodology	45
4.1	Simulation Using Multiphysics Comsol	45
4.1.1	Sitting Up The Model Environment	45
4.1.2	Creating Geometrical Object	45
4.1.3	Material Parameters	45
4.1.4	Defining The Physics Boundary Condition	46
4.1.5	Creating The Mesh	46
4.1.6	Simulation	46
4.2	Polytec Laser Scanning Vibrometer	46
4.2.1	Electronic Unit	47
4.2.2	Scanning Vibrometer Head Unit	47
4.3	Measurement	49
4.3.1	Performing Scan Measurement Of S.M.R. In Air	49

5	Results And Discussion	51
5.1	Simulation	51
5.1.1	Simulating 500-55-Z Filled With Air	52
5.1.2	Simulating 500-55-Z Filled With Liquids	53
5.2	Mechanical Characterization	53
5.2.1	Frequency stability analysis: Allan's Deviation	55
5.3	Measurement of liquids with different density	57
5.4	Evaluation of the SMRs performance and comparison with the simulation data	60
5.4.1	Simulation Micro Resonator	60
5.4.2	Experimental Results	60
6	Conclusion And Recommendation	63
6.1	Conclusion	63
	Bibliography	65
	List of Figures	67
	List of Tables	69

Chapter 1

Introduction

1.1 Origin Of Microcantilever

Micro-mechanical sensor is a form of sensor that is sensitive to changes in mechanical properties. The most popular mechanical sensor is the cantilever and acoustic sensor. These mechanical sensors play an important role in the detection of molecules. In 1968 a publication by Wilfinger [36] made the scientific community aware of the fact that adsorbed molecules were able to induce bend or a change in resonance frequency when the silicon beam was used as a sensor [22]. Wilfinger's publication further explained that large silicon cantilever structure with the of dimension of $500\mu m \times 30\mu m \times 8\mu m$ could be used as a sensor. The actuation associated with the microcantilever used by Wilfinger was achieved by means of a localized thermally expanded piezoresistor. This was located close to the cantilever support in order to generate a temperature gradient which drives the cantilever at resonance. Two decades later, the advent of the atomic force microscopy was able to utilize the cantilever in commercial product. Ever since the discovery of the atomic force microscopy in 1986, the micro-fabrication of cantilever have triggering immense research for it's used as a sensor. In 1994 for instance Itoh and Suga[19] demonstrated that by sputtering *ZnO* thin film sandwiched between two electrode. This cantilever can be used for detecting the change in resistance associated with the electrode. This was resulted in the static deflection of the cantilever. Thundat [29] also demonstrated that the resonance frequency associated with the dynamic mode of the microcantilever was influenced by the ambient conditions changes such as the moisture adsorption. The adsorbed analyze resulted in a resonance frequency change. These changes of frequencies were due to mass loading or adsorption induced changes on the cantilever and thus shifting the resonance frequencies to the left.

1.2 Operating Modes

A microcantilever sensor is a versatile platform for the investigation of various samples properties and it offer the possibility to follow the reaction occurring on it's surfaces. A classical example of this reaction was performed by Thundat [29] when the cantilever surface was coated with hygroscopic material such as phosphoric acid and gelatin. This aided the cantilever to sense water vapor at picogram mass resolution. The microcantilever can be operated in two important modes.

1.2.1 Static Mode

The static mode deals with the change in the microcantilever z- displacement which is due to either a change in load or the change in the intrinsic stress. In conclusion it can be said that the gradual bending of the microcantilever with any stress induced stimulant is referred to as been operated in static mode. Various environmental conditions can deflect the cantilever in it's static mode. These environmental conditions includes vacuum, ambient moisture and liquids. In static mode the fundamental issue is related to how the cantilever is deflected due to the presence of the stress induced stimulant. In a gaseous environment, the molecular analyte are adsorbed onto the functionalized sensing surface to form a molecular layer. This will occur provided the molecule have a high affinity for the surface. Polymer sensing layers as shown in Figure 1.1 must be able to show the high selectivity to the molecules in the environment. The molecules in the environments are able to diffuse onto the polymer layer at different rate. The diffusion mainly depends on the size and solubility of the molecules in the polymer layers. The first example of the static operation is the temperature measurement using the bimetallic effect. A cantilever which consist of two layers with different materials is sensitive to temperature variation, mainly because of the different thermal expansions of the metals. This leads to a thermally induced

stress which in the end leads to a subsequent static deflection of the beam [30]. The readout mechanism of most cantilever's operating in static mode is a piezoresistive readout microcantilever. This piezoresistive readout mechanism consist of whealstone bridge circuit with three reference of adjustable resistor. If the micro cantilever bends the piezoresistor changes it's value and current will flow between the two branches of the whealstone bridge. The current is converted via a differential amplifier into a voltage which is proportional to the deflection value in it's static mode.

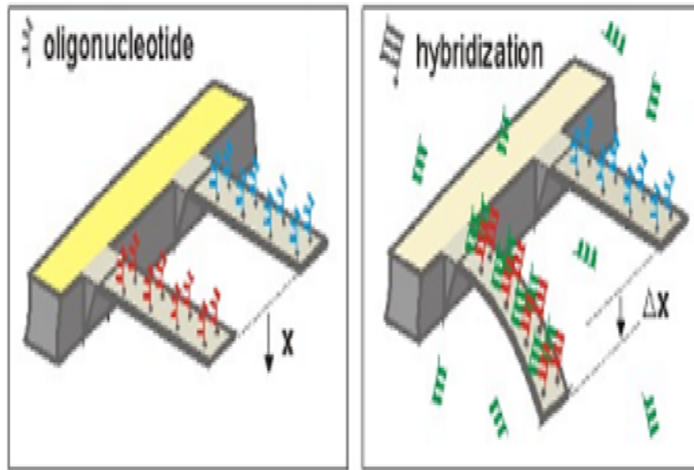


Figure 1.1: Operation scheme of a cantilever sensor based on static mode detection. A DNA hybridization is shown in the above experiment: The sensor's output is the cantilever deflection. [31].

1.2.2 Dynamic Mode

The dynamic mode of operation occurs when there there is a shift in the frequency whenever an amount of mass is absorbed by the cantilever. Since the dynamic operation mode Figure 1.2 will be the core of the experimental part of this thesis, this topic will be examined extensively form a theoretical point of view in the next Chapter. In this section the main features and physical detection principles will be investigated. Important information about the amount of molecules adsorbed can be obtained

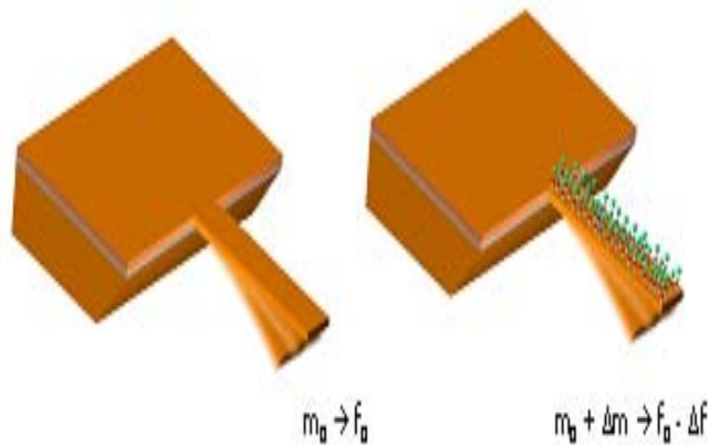


Figure 1.2: Operation scheme of cantilever based on dynamic operational mode. Mass variations of the oscillator are related to the resonance characteristic of the structure.

from the oscillating frequency of the microcantilever. Molecules on the surface might be exchanged with molecules from the environment at dynamic equilibrium. In the dynamic mode, mass changes can be

determined accurately by tracking the eigenfrequency of the microcantilever during mass adsorption or desorption. The frequency equals the resonance frequency of an oscillating microcantilever if its elastic properties remain unchanged during the molecule adsorption/desorption process and damping effects are negligible. This operation mode is called the dynamic mode and the microcantilever is used as a microbalance. The added mass onto the cantilever surface will only result in the cantilever's frequency being shifted to a lower value.

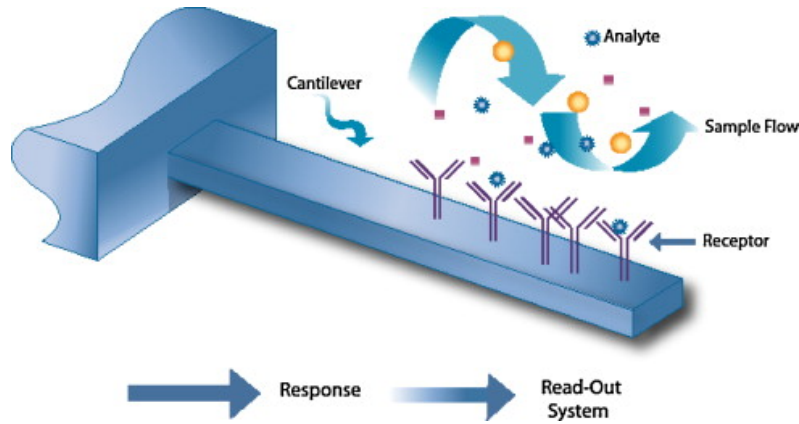


Figure 1.3: A figure illustrating the dynamic-mode cantilevers .

The international union of pure and applied chemistry defines a biosensor as a device that uses specific biochemical reaction mediated by isolated enzymes, immune systems and a whole cells to detect chemical compounds. According to Blake's [6] publication the dynamic mode cantilevers responds to surface biochemical interaction through resonant frequency. The Figure 1.3 illustrates dynamic mode cantilever's responds to surface biochemical interaction through resonant frequency change caused by a change in it's mass or stiffness. Although the resonant frequency is used to discern molecular binding a variety of different resonant modes may be used for sensing.

1.3 Suspended Micro And Nano Resonator

The suspended microchannel resonator is a device that measures the particle's masses as they flow through the narrow channel. This mass sensor device consist of a fluid filled microchannel etched in a silicon cantilever which vibrates inside a vacuum cavity [24]. According to Selim Olcum the basic idea is when a particle or cell flows through the channel, the cell or particles mass slightly alters the cantilever vibration frequency. The mass of the of the particle or cell can be calculated using the change in frequency using the expression below

$$\frac{\partial f}{\partial m} = \frac{f}{2m^*} \quad (1.1)$$

The above Equation 1.1 is under the assumption that we are dealing with the small mass approximation and operating in the dynamic mode. The sensitivity of suspend microchannel resonator comes with it's inherent issues. This is because in pursuit for higher sensitivity the dimension of the suspended micro resonator have been greatly scaled down. The downscaling of the mass sensor have not only increased the mechanical stiffness but also increased the natural frequency. This approach present new challenges which needs to be addressed for implementing high throughput transduction system [29]. There are other important factors which attenuate the mechanical mass sensor performance in a liquid environment. For instance whenever a resonator is immersed in a very viscous liquid. The resonator encounters an over-damped response of the resonator. This generates a rapid dissipation of energy which eventually degrades the frequency resolution and sensitivity. The solution of the above limitation was proposed by Burg in [7], which involved integrating a fluidic channel into a mass microcantilever which became known as the suspended microchannel resonator(SMR). The integration of the fluidic channel helped to avoid damping and viscous drag generated by the fluidic environment [7]. This (SMR) mechanical mass sensor has emerged to be an alternative for label free detection method in comparison to other sensing techniques like surface plasmon resonance and Quartz crystalline micro-resonator(QCM).

The actual goal of the SMR was to offer an advanced sensing platform which requires small volume consumption of the sample. In addition to the above goal is the fact that the SMR is coupled with an increase in sensitivity. There is also the ability to scale down the technology in order to extend

their application in bioanalytical application [28]. In general the bioanalytical SMR can be operated in two operational modes: affinity-based and the flow through detection mode as shown in Figure 1.4. The affinity based detection deals with biofunctionalization procedures which provide specific capture of molecules into the inner microchannel walls of the SMR while replenishing the microchannel. On the contrary the flow through detection allows the identification of fluids and small entities that are streaming through the microchannel. In both modes the sensitivity is proportional to the resonant frequency which in turn is inversely proportional to the effective mass of the sensor[9].

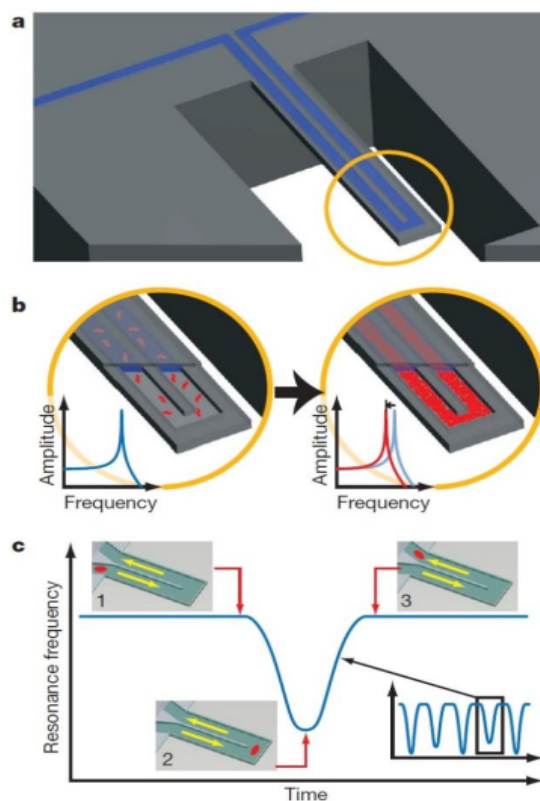


Figure 1.4: Representation of the two operational modes of SMR A. The SMR translates the mass change into changes of frequency while the fluid continuously flow through the channel B. Is a surface adsorption mechanism in which the molecules binds to the channel. C. The particle that flow the SMR without binding to the surface can be observed depending on their position in the channel. [7]

Ever since the first functionalization principle of SMR device was demonstrated many effort have been made improve their frequency response and their resolution technologically in order a achieve excellent responsivity for mass spectrometry. In 2006, [8] operated the SMR device under vacuum condition with the addition of glass frit bonding for hermetic packaging. This hermetic SMR device operated at a pressure of approximately 1 Torr generated a measured Q-factor which was five time better than the one measure in air ($Q = 90$). This was achieved thanks to the frequency resolution been improved by using the electrostatic actuation of the resonator. This resulted in the generation of biomolecule recognition of about 0.01gcm^{-2} and outperformed the mass adsorption resolution of contemporary label free sensors. A year afterward this same SMR was successfully used to to weigh nanoparticles, bacterial cell (*E. Coli* and *B. Satillilis*) and adsorbed proteins in the SMR flow detection technique. The SMR's ability to weigh single nanoparticles was achieved by designing the SMR to sustain higher frequencies by diminishing it's dimension. A very thin frequency spectrum were depicted by incorporating a getter layer into the packaging of the device. This improved the frequency stabilities and resolution of the detection system.

1.4 Application Of SMR

Under this premise it is known that SMR devices have opened the gate for a broad range biological application for measuring the mass, volume, density and size of polystyrene particles, *Escherichia coli* bacteria and human red blood cell. These biological samples were measured with the with density

resolution down to 10^{-4}gcm^{-3} [7]. In 2010 femtogram detection of growing rate of individual cells such as *Bacillus subtilis*, *Escherichia coli* and even mouse lymphocyte was achieved by using the a buoyant mass methodology with an SMR device [17]. An accurate pressure control approach system was implemented in order to control the sample delivery to allow consecutive buoyant mass measurement of single cells. In another breath the improvement on the surface was obtained by functionalization of the embedded microchannels of SMR device have been used to detect biomarker in undiluted serum. Surface binding assay based on zwitterionic polymer in an undiluted serum was found to have a detection limit of around 10ng/mL. Grover in [18] provided a significant insight in understanding the cell state during drug delivery treatment. In the approach single cell were weighed using two fluids having different densities. Applying the principle in order to linearize the relationship between the buoyant mass and the fluid density in order to forecast the mass, volume and density of single cell at a cell rate of 500 cell per hour. The precision in their density was about 0.001g/mL. Bryan in [9] developed a similar dual SMR for the determination

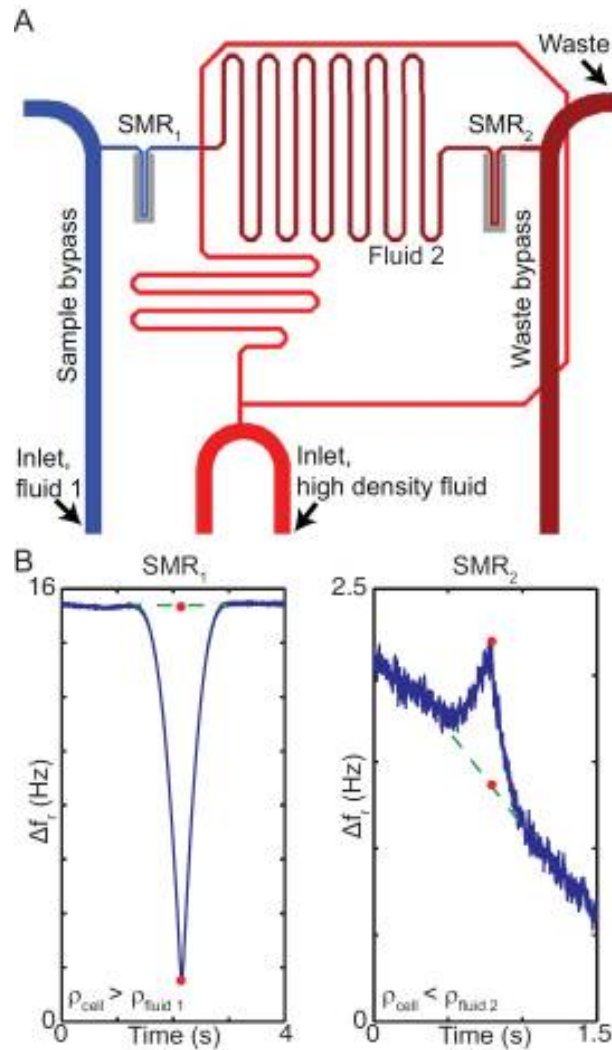


Figure 1.5: Representation of the two SMR having different fluids that used in the Groove's article [18]

of mass, volume and density but the only difference was that their device utilized serpentine in it's fluidic channel. In that manner the single were weighed in the two devices during a single sample injection as shown in Figure 1.5 above.

Among the different types of resonators, the hollow channel resonators have emerged as a potential platform for measuring minute analyze in liquids flow through an embedded channel with exceptional responsivity. The hollow channel resonator have allowed for high resolution mass measurement for analyte in liquids especially biological molecules. The hollow channel resonator (HCR) platform is applied in sensing the analyze properties in it's native environment and has been used for sensing the mass, volume and density of cancer cell in their physiological conditions. The capillary electrophoresis was combined with the hollow nanochannel resonator to overcome the low ionic conductivity of the HNR as shown in Figure 1.6. This aided the configuration shown above to be used as a mass spectrometer. The analyze flow

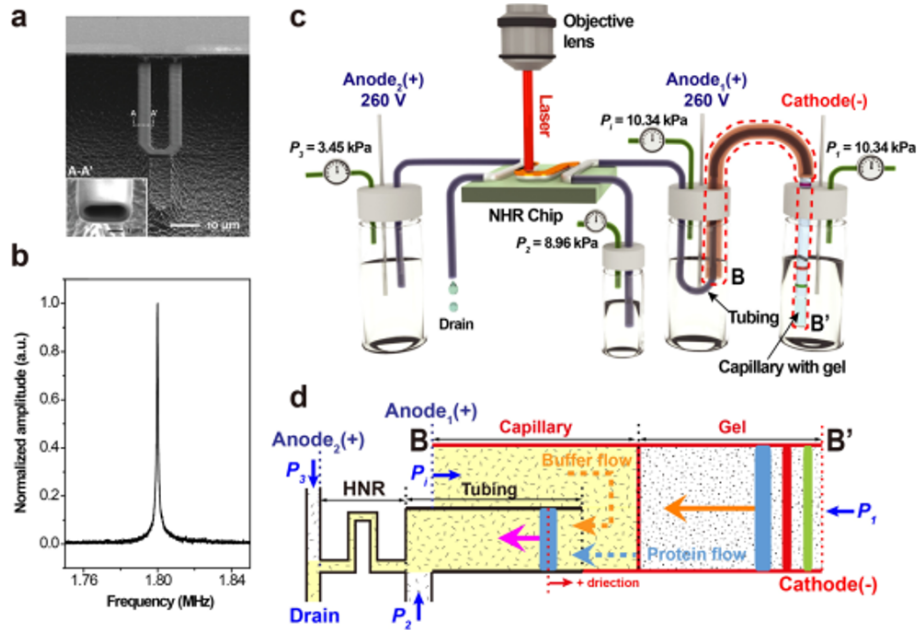


Figure 1.6: A figure illustrating a classical HNR that was used as electrophoresis assisted time of flow mass spectrometry.

through the conductive embedded channel was achieved thanks to the rightful use of the hydrodynamic pressure which override the electromotive force.

1.5 Microfluidic Resonators Fabrications

When MEMS technology came to the limelight it was thanks to the utilization of silicon based substrate. The excellent electrical and thermal properties coupled with its high throughput made silicon a potential candidate for the fabrication of MEM devices. The silicon based micro technology was accomplished based on the integration of additive and subtractive fabrication processes. These two processes add and remove silicon material layer by layer. The fabrication process of all MEMS devices including the resonators were accomplished using these two essential processes: the surface and the bulk micromachining. Bulk micromachining deals with manufacturing the substrate to build up microstructures. Normally the patterns are generated by an etching process while the desired microstructures patterns are transferred onto the substrate by means of photolithography. Photolithography is an optical technique that makes copies of 2D designs from the mask to the substrate using the UV light. When the U.V light is exposed to the photosensitive resist which is on top of the substrate. The photoresist is chemically modified by the UV light. The photoresist is removed thereafter by some dry and wet etching techniques. The most common dry etching process is the reactive ion etching (RIE) which selectively removes the exposed material by bombardment of ion. Wet etching on the other hand is carried out with the whole substrate being immersed in the etchant solution just in order to eliminate those materials that have high selectivity to the etchant solution. Surface micromachining deals with the sequential fabrication steps on the substrate surface. Conventionally the microstructure resonators are archived by using a combination of sacrificial and structural material in order to develop the final structure. This means that using photolithography and dry etching processes the final structure is generated. This final structure could be a released cantilever or a hollow microchannel resonating structure. Another important step in MEMS microscaled resonating structure fabrication is the packaging of the device. A well packaged device is that device which are normally protected from external noise, moisture and electromagnetic fields.

The vacuum package suspended microchannel resonator mass sensor according to Burg and Manalis [8] was fabricated with polysilicon being used as a sacrificial layer of silicon nitride. The silicon nitride was fabricated by the low pressure chemical vapor deposition. The first stage involved the etching of a channel of depth of about $1 \mu\text{m}$. The wafer was then coated with a low stress LPCVD using a 10:1 ratio of SiCl_2 and NH_3 at a temperature of 77°C . The associated pressure was 250 mtorr using the SVG thermal reactor. The resulting structure was subsequently followed by the deposition of the $1.5 \mu\text{m}$. The

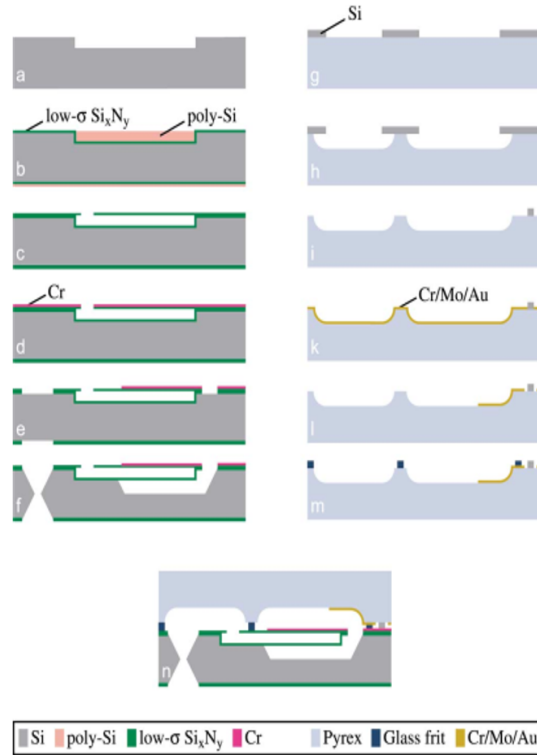


Figure 1.7: The fabrication and packaging process of a suspended microchannel resonator [8].

polysilicon was thereafter removed by the chemical mechanical polishing so that only the etched feature remained filled as shown in Figure 1.7b. After this planarization another layer of low stress LPCVD silicon nitride was deposited to close the polysilicon filled microchannels. The second stage involved the generation of accessible hole with dimensions of $60\mu\text{m} \times 30\mu\text{m}$. were etched in the SiN_x with a hot KOH. In our quest to avoid the problem of stiction associated wet etching a diaphragm of dimension $20\mu\text{m} \times 800\mu\text{m}$. of SiN_x was developed Figure 1.7c. In the third stage was related to the deposition of a 50nm layer of Chromium(Cr) by the ion beam deposition as shown in Figure 1.7d. The purpose of the chromium layer is to provide a high reflectivity for optical readout. The same chromium was patterned in order to minimize the stress on the resonator. Thereafter there was the removal of metal from all areas that have the possibility of making contact with the fluid. The fourth stage deals with the subsequent dry etching through the SiN_x just in order to define the resonators outlines and location. This also helped in the definition of the fluid vias as shown in Figure 1.7e. The bulk micromaching was performed just in order to release the resonator by using the etchant TMAH (tetra methyl ammonium hydroxide) The etchant TMAH was also used because of it's compatibility with the chromium metalization as illustrated in Figure 1.7f. The fifth stage involved the usage of the glass wafer for packaging by anodically bonding the silicon and glass wafer. The pattern that is seen in Figure 1.7g was achieved by using the etchant HF. The sixth stage dealt with the help of the mask generated above to perform a deep reactive ion etching DRIE which resulted in the undercut as shown in Figure 1.7h. The same DRIE was used to remove the Islands of silicon leaving a sparse distribution of silicon. This sparse distribution of silicon was left mainly because it was going to form an important part of the bonding. Finally a thin film of gold is deposited onto the structure as it's adhesive layer as shown in Figure 1.7k. The two separate component are bonded by using the glass frit bonding as shown in Figure 1.7k.

The second fabrication technique deals with the fabrication of micro-capillary tube resonator according to Donghyuk et. al. [13]. This micro-capillary is achieved by a simply pulling process of borosilicate glass. The fabrication process is most convenient in places where there is no available cleanroom facility. The laser heated pipetted puller defines the micro-capillary tube through sequential heating and pulling processes which locally stretch the middle section of the glass capillary while the cross section is maintained as shown in Figure 1.8. The pipette is completely different from the typical use of the pipette. Furthermore it could be wound up and make a 360° loop as shown in Figure 1.8. With the unpulled section at both sides. This will facilitate interfacing with standard fluidic components. First

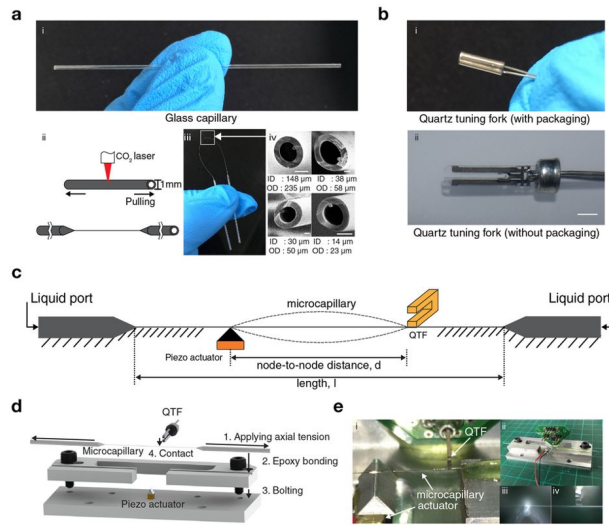


Figure 1.8: The fabrication of a microcapillary tube resonator [13].

a 0.3N axial tension is applied to the unpulled structure using a tension gauge. The applied tension is maintained with the microcapillary is pulled into the final structure.

Chapter 2

Theory

2.1 Resonance Frequency

Nanomechanical resonators of beams and bridges are continuum mechanical structures. In this section the eigenmodes of such ideal lossless continuum mechanical structures are studied by basic analytical models. Explicit resonance modes of a damped continuum mechanical structure are ideally portrayed by the lumped-element model. In this section, the eigenmodes of the most widely recognized continuum mechanical structures which are evaluated. Thereafter linear coupled, nonlinearly damped and driven resonators are examined using the lumped element model [34]. At the eigenfrequency of a ideal(lossless) mechanical structure as per the equipartition theorem states that the kinetic energy of a particular mechanical vibration is equivalent to the potential energy stored in the individual vibrational deformation of the structure. Continuum mechanical structure have numerous such vibrational modes which are called eigenmodes at which this resonance process occurs.

At the eigenfrequency the total energy associated with the mechanical framework is passed forward and backward unendingly between the kinetic and potential energy. Once the energy is added by for instance a kick such a system would definitely oscillate at it's eigenfrequency with a constant vibrational amplitude. In a genuine mechanical structure anyway not the whole energy is commutating among the kinetic and potential energy however a little piece of the energy is lost at each cycle of vibration. There are various mechanisms by which the energy can be lost and this is also examined in this section. Consequently a genuine mechanical structure will oscillate for a limited amount of time until all the energy that initially entered the system have all been lost. In genuine mechanical structures with inherent losses these eigenmodes component are called **resonance**.The predominant frequency at which the energy is commutating between the kinetic and potential energy is called the **resonance frequency**.The resonance frequency is normally close (somewhat lower) to the eigenfrequency of a similar micro mechanical structure without losses. According to S. Schmid [34], the resonance frequency of the micro and nanomechanical systems is typically estimated using the respective eigenfrequency computed using the analytical models of finite element method (FEM) simulation.

2.1.1 Eigenmodes of Ideal Continuum Mechanical Structures

In this section, analytical models are introduced to describe the free and lossless(conservative) vibration of continuum mechanical structures typically used as that of micro- and nanomechanical resonators. Bending vibrations of "one-dimensional" resonators such as beams , are discussed in this section. The string is a special case of a doubly clamped beam that is under tensile stress, such that the effect of the tensile stress is dominating over the beams bending stiffness normally called the flexural rigidity. In other words, the difference between beams and strings lies in the way potential energy is stored. While in beams the potential energy is stored in the elastic bending, in strings it is stored in the work done against the strong tensile stress during deflection. The classical way to find the eigenmodes of a continuum mechanical structures is by deriving the differential equation of motion, which can be obtained by equalizing all the forces (inertial and elastic) acting on an infinitesimally small piece of structure (Newton's third law). In this way it is readily possible to derive exact solutions for many simple and idealized continuum mechanical structures such as beams.

Rayleigh's method is a useful tool to obtain a good approximation for the fundamental eigenfrequency of a conservative system (a system without loss of energy). This Rayleigh's method is based on the complete commutation of the energies,which means that the kinetic and potential energy must commute

as stated by the (equipartition theorem) explained previously. This theorem assumes that the maximum kinetic energy is equal to the maximum potential energy.

$$W_{Kin}^{max} = W_{Pot}^{max} \quad (2.1)$$

The potential and kinetic energy of a double clamped beam is shown in [Table 2.1](#) According to the above

Members	Potential Energy	Kinetic Energy
Double Clamped Beam	$\frac{EA}{8} \int_0^l \left(\frac{\partial^2 u}{\partial x^2} \right)^2 dx$	$\frac{A\rho}{2} \int_0^l \left(\frac{\delta^2 u}{\delta t^2} \right)^2 dx$

Table 2.1: An table illustrating the potential and kinetic energies of a double clamped beam

table it is obvious that in order to compute either the potential or kinetic energy the structure's specific mode shape $U(x,y,t)$ must be known. The separation of variable makes it possible to separate the spatial and the temporal part as shown in [Equation 2.2](#).

$$U(x, y, t) = U(x, y) \text{Cos}(wt) \quad (2.2)$$

Where $U(x,y)$ is the spatial mode shape function which gets modulated by the temporal sinusoidal function $\text{Cos}(wt)$ having an angular velocity w . The spatial mode shape function obtain a maximum value when the temporal function is unity as shown in [Equation 2.3](#).

$$\text{Max} \{ \text{Cos}wt \} = 1 \quad (2.3)$$

It must be emphasized that the potential energy maximum is readily given by [Equation 2.4](#).

$$W_{pot}^{Max} = \text{Max} \{ W_{pot}(U(x, y, t)) \}, \quad (2.4)$$

$$W_{pot}^{Max} = W_{pot}(U(x, y)).$$

The kinetic energy is also given [Equation 2.5](#)

$$W_{Kin} \propto \left\{ \frac{\partial U(x, y, t)}{\partial t} \right\}^2 \quad (2.5)$$

The ansatz associated with the mode shape function is expressed as in [Equation 2.2](#) at the maximal kinetic energy can be expressed as:

$$W_{kin}^{Max} = \text{Max} \{ W_{kin}(U(x, y, t)) \},$$

$$W_{kin}^{Max} = \frac{\partial^2}{\partial t^2} (U(x, y) \text{Cos}(wt)), \quad (2.6)$$

$$W_{kin}^{Max} = \omega^2 W_{kin}(U(x, y)).$$

Substituting [Equation 2.4](#) and [Equation 2.6](#) into [Equation 2.1](#) we obtain the expression in [Equation 2.7](#)

$$W_{pot}^{Max} = \omega^2 \{ W_{kin}(U(x, y, t)) \},$$

$$W_{pot}(U(x, y)) = \omega^2 W_{kin}(U(x, y)), \quad (2.7)$$

$$\Omega^2 = \omega^2 = \frac{W_{pot}(U(x, y))}{W_{kin}(U(x, y))}.$$

The above [Equation 2.7](#) provides us with the possibility of computing the eigenfrequency given a suitable displacement mode function $U(x,y)$. This Rayleigh's [Equation 2.7](#) method yields the exact eigenfrequency if the exact mode shape is known. Usually the exact displacement mode shape function remains unknown. The best practice however is to make an appropriate approximation which satisfy all the boundary conditions. A common practice is to use the displacement function of the corresponding static structure

of interest due to uniform loading. The Rayleigh's method explained above gives a decent results at fundamental eigenfrequency but in order to have a more accurate results at higher modes, the Rayleigh's method is combined with the **Ritz's method**. The Ritz's method is a variational method that is used to approximate various mechanical boundary values problems. The Ritz's method in principle is based on the minimization of the total potential energy of a mechanical system [32]. The minimum energy is found by varying free variables of test solution which obeys all the boundary conditions. The combined method (Rayleigh Ritz) is used to approximate the eigenfrequency of a specific mechanical boundary value problem. According to the Ritz's method associated with n number of free variables C_i are introduced into the spatial mode shape function $U(x,y)$.

$$U(x, y) = \sum_{i=1}^n C_i U_i(x, y) \quad (2.8)$$

The set of variable C_i which must be taken in order to minimize the total energy in given mechanical structure is the same set of co-efficient that must be found in order to have minimum eigenfrequency if and only we apply the Ritz's method to the so called Rayleigh's quotient as shown in Equation 2.7. The Equation 2.9 was obtained by substituting Equation 2.7 into Equation 2.8

$$\frac{\partial \omega^2}{\partial C_i} = \frac{\partial}{\partial C_i} \left\{ \frac{W_{pot}(U(x, y))}{W_{kin}(U(x, y))} \right\} = 0 \quad (2.9)$$

By applying the quotient derivative rule to Equation 2.9 we are able to obtain the the expression Equation 2.10.

$$\frac{\partial}{\partial C_i} \{ W_{pot}(U(x, y)) - \omega^2 W_{kin}(U(x, y)) \} = 0 \quad (2.10)$$

Substituting the Equation 2.8 into Equation 2.10 yields a homogeneous linear system of equations of n variables which can be written as:

$$M_n(\omega) C_i = 0 \quad (2.11)$$

The $M_n(\omega)$ is the square matrix of the order n multiplied by the C_i values of the vector C_i . In order to get the non-trivial solution, the determinant of this square matrix has to be equal to zero as shown in Equation 2.12.

$$\det(M_n) = 0 \quad (2.12)$$

The Equation 2.12 is important mainly because it results in the characteristic equation which yields the eigenfrequencies ω_i It is clear from Equation 2.8 that Rayleigh-Ritz method for n=1 reduces to the Rayleigh method.

2.2 Free Bending Vibrations Of Beams

The eigenmodes problem of bending beams is a prominent case that can be solved exactly. The model is based on the bending theory which was proposed by the swiss mathematicians Leonard Euler and Daniel Bernoulli in the eighteenth century. The bending behavior of beams is modeled under the assumption $\left(\frac{l}{h} > 10\right)$ as shown in Figure 2.1. It must be emphasized that the rotational inertia and the shear

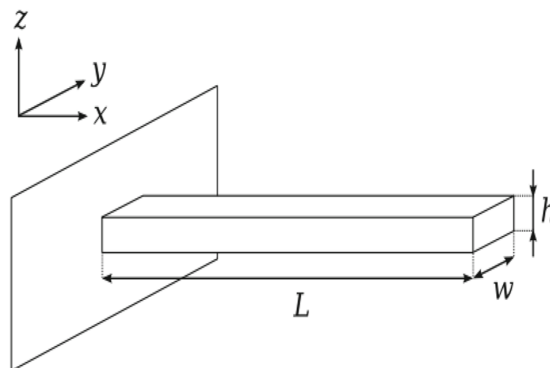


Figure 2.1: This figure illustrate the beam. [34]

deformation is completely neglected. The equation of motion of the slender beam can be derived by means of the equilibrium of forces on an infinitesimal piece of beam. It is also assumed that a linear elastic material are able to generate a small deflection $U(x,y)$.The Euler Bernoulli's equation is given by

$$\rho A \frac{\partial^2 U(x,y)}{\partial t^2} + EI_y \frac{\partial^4 U(x,y)}{\partial x^4} = 0 \quad (2.13)$$

Where ρ is the mass density. A is the cross sectional area, E is the young modulus and the I_y Is the geometric inertia.

The solution to the above differential equation [Equation 2.13](#) is a superposition of the normal modes which as we all know can be separated into position dependent terms and time dependent terms through the separation of variables [\[5\]](#).

$$U(x,y) = \sum_{n=1}^{\infty} U_n(x) \text{Cos}(\omega t) \quad (2.14)$$

Where ω is the frequency of motion and n denotes the modal number. A general solution to the displacement modal function is $U_n(x)$ which can be expressed as [Equation 2.15](#)

$$U_n(x) = a_n \text{Cos}(\beta_n x) + b_n \text{Sin}(\beta_n x) + c_n \text{Cosh}(\beta_n x) + d_n \text{Sinh}(\beta_n x) \quad (2.15)$$

The β_n in [Equation 2.15](#) represent the wavenumber. The first two terms in [Equation 2.15](#) are the trigonometric functions which are coming from the standing wave associated with the beam whiles the remaining two hyperbolic terms are coming into the equation as a result of the clamping of the beam. It could be concluded from the [Equation 2.15](#) that the beam vibrate with a certain vibrational mode with each mode have a distinct modal shape.

$$U(x,t) = \sum_{n=1}^{\infty} \text{Cos}(\omega t), \quad (2.16)$$

$$\frac{\partial^2 U}{\partial t^2} = -\omega^2 U(x,t).$$

The [Equation 2.16](#) is providing us with the second partial derivate with respect to time, however there is the need to find the fourth partial derivation with respect to space. Performing the fourth partial derivative with respect to space of [Equation 2.15](#) obtain [Equation 2.17](#)

$$\frac{\partial^4 U(x)}{\partial x^4} = \beta_n^4 * (a_n \text{Cos}(\beta_n x) + b_n \text{Sin}(\beta_n x) + c_n \text{Cosh}(\beta_n x) + d_n \text{Sinh}(\beta_n x)), \quad (2.17)$$

$$\frac{\partial^4 U(x)}{\partial x^4} = \beta_n^4 U(x,t).$$

Substitute [Equation 2.16](#) and [Equation 2.17](#) into [Equation 2.13](#). The below expression is obtained:

$$\rho A (-\omega^2 U(x,t)) + EI_y (\beta_n^4 U(x,t)) = 0, \quad (2.18)$$

$$\rho A \omega^2 = EI_y \beta_n^4.$$

$$\Omega = \omega = \beta_n^2 \sqrt{\frac{EI_y}{\rho A}}$$

The final results of [Equation 2.18](#) can be further simplified by defining a quantity C_E which is called the wave-velocity in the elastic wave thus modifying [Equation 2.18](#) into [Equation 2.19](#) as shown below.

$$C_E = \sqrt{\frac{E}{\rho}}, \quad (2.19)$$

$$\Omega = \omega = \beta_n^2 C_E \sqrt{\frac{I_y}{A}}.$$

Assuming that the structure under consideration is of a rectangular cross section with beam height of h the geometric inertia can be expressed as

$$I_y = \frac{Ah^2}{12} \quad (2.20)$$

Substituting the Equation 2.20 into the Equation 2.19 the expression Equation 2.21 can be obtained:

$$\Omega = \omega = \beta_n^2 C_E \sqrt{\frac{I_y}{A}},$$

$$\Omega = \omega = \beta_n^2 \sqrt{\frac{EAh^3}{12\rho Ah}}. \quad (2.21)$$

$$\Omega = \omega = \beta_n^2 \sqrt{\frac{Eh^3}{12} \frac{1}{\rho h}}.$$

With the final result of Equation 2.21 in view we can define the flexural rigidity of a square beam which is expressed as Equation 2.22.

$$D_E = \frac{Eh^3}{12} \quad (2.22)$$

The final expression of the eigenfrequency associated with the Euler Bernoulli equation is expressed as Equation 2.23

$$\Omega = \omega = \beta_n^2 \sqrt{\frac{D_E}{\rho h}} \quad (2.23)$$

The Euler Bernoulli beam theory assumes that a thin and long beam is used. If the width to height ratio becomes greater than 5 then the flexural rigidity of the Euler-Bernoulli beam needs to be changed to the flexibility rigidity of a plate as shown in Equation 2.24

$$D_p = \frac{Eh^3}{12(1-\nu^2)} \quad (2.24)$$

Where ν is the Poisson ratio which takes account of the dilation of the beam when an axial strain is applied. In this section we only need to find the wavenumber associated with specific eigenmodes of the bridge. This is by first of all finding the unknowns coefficients (a_n, b_n, c_n, d_n) as shown in Equation 2.16 applying the appropriate boundary condition of the doubly clamped beam or bridge.

2.3 Bridges

Bridge are specialized beams in the which both ends are fixed. The associated boundary conditions is given as shown Equation 2.25

$$U_n(0) = U_n(L) = \frac{\partial U_n(0)}{\partial x} = \frac{\partial U_n(L)}{\partial x} = 0 \quad (2.25)$$

The Equation 2.25 is an equation that is demanding that there is no net displacement and slope at both ends of the doubly clamped beam. The application of these boundary condition above only generate a system of linear equation of the fourth order which is expressed as a matrix in Equation 2.26.

$$\begin{bmatrix} 0 \\ 0 \\ 0 \\ 0 \end{bmatrix} = \begin{bmatrix} 1 & 0 & 1 & 0 \\ 0 & 1 & 0 & 1 \\ \sin(\beta_n L) & -\cos(\beta_n L) & \sinh(\beta_n L) & \cosh(\beta_n L) \\ \cos(\beta_n L) & \sin(\beta_n L) & \cosh(\beta_n L) & \sinh(\beta_n L) \end{bmatrix} \begin{bmatrix} a \\ b \\ c \\ d \end{bmatrix} \quad (2.26)$$

Setting the determinant of the above matrix in Equation 2.26 to zero we obtain the Equation 2.27.

$$\cos(\beta_n L) \cosh(\beta_n L) - 1 = 0 \quad (2.27)$$

With the solution that have been obtained in Equation 2.27. If we assume that $n=1,2,3$ then in that case we can find out that $\beta_1 L = 4.7300, \beta_2 L = 7.8532, \beta_3 L = 10.9956$. The frequency equation's solution associated with the bridge is illustrated in Figure 2.2. The associated mode shape function of the bridge

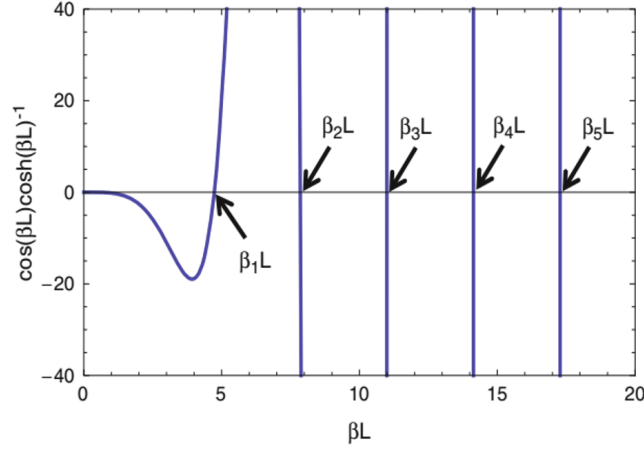


Figure 2.2: A figure illustrating the plot of the roots associated with the frequency equation shown in Equation 2.27

can be obtained from the boundary condition as shown in Equation 2.25. According to the first boundary condition we obtain a expression almost similar to the case of the cantilever.

$$U_n(0) = 0 : a + b = 0,$$

$$\frac{\partial U_n(x=0)}{\partial x} = 0 : b + d = 0. \quad (2.28)$$

$$\frac{\partial^2 U_n(L)}{\partial x^2} = 0 : \frac{b_n}{a_n} = \frac{-\text{Cos}(\beta_n L) - \text{Cosh}(\beta_n L)}{\text{Sin}(\beta_n L) - \text{Sinh}(\beta_n L)}$$

The significant observation that could be seen is that by applying the first and second boundary condition. The final result is express in Equation 2.28. The application of the first and second boundary condition have also considerably reduced the Equation 2.15 is reduced to Equation 2.29

$$U_n(x) = a(\text{Cos}(\beta_n x) - \text{Cosh}(\beta_n x)) + b(\text{Sin}(\beta_n x) - \text{Sinh}(\beta_n x)) \quad (2.29)$$

With the Figure 2.3 we are observing the one dimensional first four bending modes of a double clamped beam. Applying the third boundary condition the coefficient of a_n and b_n is obtained as illustrated below:

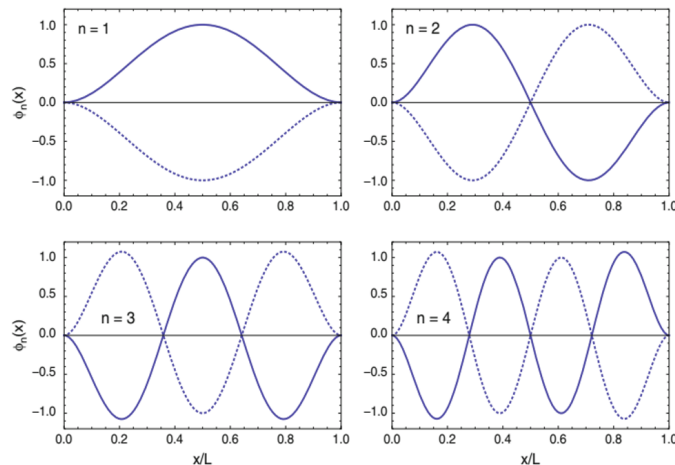


Figure 2.3: A figure illustrating the first four bending modes of the double clamped beams.

$$\frac{\partial^2 U_n(L)}{\partial x^2} = 0, \quad (2.30)$$

$$\frac{b_n}{a_n} = \frac{-\text{Cos}(\beta_n L) - \text{Cosh}(\beta_n L)}{\text{Sin}(\beta_n L) - \text{Sinh}(\beta_n L)}$$

The logical conclusion that can be found is that the coefficient b_n is given shown in [Equation 2.31](#)

$$b_n = -a_n \left[\frac{\text{Cos}(\beta_n L) + \text{Cosh}(\beta_n L)}{\text{Sin}(\beta_n L) - \text{Sinh}(\beta_n L)} \right] \quad (2.31)$$

Substituting [Equation 2.31](#) into the [Equation 2.29](#) the [Equation 2.32](#) is obtained. This [Equation 2.32](#) is the mode shape function associated with our system.

$$U_n(x) = a \left\{ \text{Cos}(\beta_n x) - \text{Cosh}(\beta_n x) - \left[\frac{\text{Cos}(\beta_n L) + \text{Cosh}(\beta_n L)}{\text{Sin}(\beta_n L) - \text{Sinh}(\beta_n L)} \right] * (\text{Sin}(\beta_n x) - \text{Sinh}(\beta_n x)) \right\} \quad (2.32)$$

Usually the mode shape function is expressed as a edge peak of the bridge $\phi_n(x)$ is approaching:

$$\phi_n(x) = \frac{1}{\sqrt{2}} \left\{ \text{Cos}(\beta_n x) - \text{Cosh}(\beta_n x) - \left[\frac{\text{Cos}(\beta_n L) + \text{Cosh}(\beta_n L)}{\text{Sin}(\beta_n L) - \text{Sinh}(\beta_n L)} \right] * (\text{Sin}(\beta_n x) - \text{Sinh}(\beta_n x)) \right\} \quad (2.33)$$

The [Equation 2.33](#) for $n \leq 3$ the normalized mode number is given by $n = 1, 2, 3$ the factors are given by: 0.6297, 0.6626, 0.7112.

2.4 Lumped Element Resonator Models

In this section a more detailed behavior of resonator is going to be studied using the lumped element model which is quite different from the simple energy continuum mechanical system studied above. The mechanical vibration in physical system are associated with the periodic conversion of kinetic to potential energy and vice versa. Elastic elements such as beams are able to store potential energy in terms of deformation of energy. However if the system comes out of it's rest position it translate the potential energy into kinetic energy. This periodic energy conversion would continue forever if the present mechanical energy would not be resisted by it's dissipative forces. About the calculation of the free vibration (eigenfrequency) of the continuum mechanical resonator. As we discussed previous the idea was to dismiss the dissipation whiles the total energy at any given time remained constant. It is clear that such system are not physical and for that matter there is dissipation through many means like viscous damping, acoustic transmission, surface losses and internal dissipation. Dissipative force are often proportional to the velocity of the velocity of the vibrational movement and are most often than not as a dashpot as shown in [Figure 2.4](#). The mechanic behavior of solids is generally approximated by

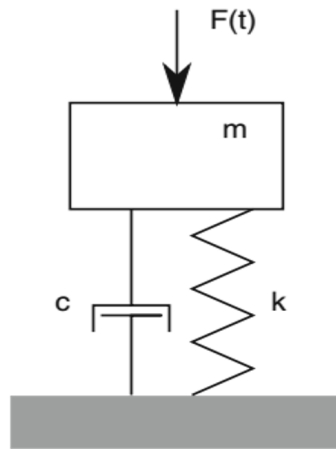


Figure 2.4: A figure illustrating the damped one dimensional oscillator with one degree of freedom [\[34\]](#).

linear relation between the continuum stress as expressed in [Equation 2.34](#)

$$\sigma = E * \varepsilon \quad (2.34)$$

Where E is the young modulus as long as the resonator is driven within the linear regime in which case for appropriate small vibrational amplitudes the dynamics of an a linear harmonic oscillator. The forced vibration of freedom can hence be modeled with a one -dimensional resonators based on a linear zero mass spring, a linear damped element and a mass as depicted in [Figure 2.4](#). Assuming a periodic driving force the second order

$$F(t) = F_o \cos(\omega t) \quad (2.35)$$

The second order equation of the resonator is expressed as:

$$m\ddot{z} + c\dot{z} + kz = F(t) \quad (2.36)$$

Where m is the total mass and K is the spring constant and c is the coefficient of the damping force. In some specific case of a non driven lumped element resonator with a damping coefficient of c the total energy of the system remains constant. In this case the resonator turns into an oscillator with vibrational amplitude which is expressed in [Equation 2.37](#)

$$z(t) = z_o \cos(\omega t) \quad (2.37)$$

During oscillation the total energy is fully swapped back and forth between kinetic (at the zero crossings) and potential (at the reversal points) energy. According to the equipartition theorem the two energies have to be equal and this yields the eigenfrequency Ω of the undamped free mechanical system which is also called the oscillator as shown in [Equation 2.38](#)

$$\Omega = \omega = \sqrt{\frac{k}{m}} \quad (2.38)$$

2.4.1 Freely Damped Resonator

In the case of a not driven system the equation of motion is as shown in [Equation 2.36](#). The equation can be reduced to homogeneous differential equation which is:

$$\ddot{z} + 2n_c\dot{z} + \Omega z = 0. \quad (2.39)$$

The associated coefficient of damping is given by [Equation 2.40](#)

$$n_c = \frac{c}{2m}. \quad (2.40)$$

Inserting the trial solution which is given by $z = z_o \exp^{\gamma t}$ into the [Equation 2.39](#) the final solution is given below [Equation 2.41](#)

$$\gamma_{1,2} = -n_c \pm \sqrt{n_c^2 - \Omega^2}. \quad (2.41)$$

The resonator's performance is defined by the ratio between n_c and Ω which is usually called the damping ratio as shown in [Equation 2.42](#)

$$\zeta = \frac{n_c}{\Omega}. \quad (2.42)$$

As seen in [Equation 2.42](#) it is known that if $\zeta \geq 1$, then the γ is real which makes the trial solution an exponential decaying. This will be the solution which is considerably referred to as been heavily damped (over damped case). In the case of a slightly damped system the $\zeta \leq 1$ which means that the γ becomes as shown in [Equation 2.43](#)

$$\gamma_{1,2} = -n_c \pm i\sqrt{\Omega^2 - n_c^2} \quad (2.43)$$

Since for a linear homogeneous ordinary differential equation the sum of linearly independent solution (real and imaginary) are also solutions and thus by applying Euler's the solution of [Equation 2.39](#).

$$Z(t) = Z_o \exp^{-\gamma \zeta t} \cos(\Omega \sqrt{1 - \zeta^2} t) \quad (2.44)$$

The [Equation 2.44](#) is indicating the resonating system which has an exponential decaying oscillation we can say that the frequency associated with the system is given by

$$\begin{aligned} \omega_{nat} &= \Omega \sqrt{1 - \zeta^2} \\ &= \sqrt{\Omega^2 - \zeta^2 \Omega^2} \\ &= \sqrt{\Omega^2 - n_c^2} \end{aligned} \quad (2.45)$$

The [Equation 2.45](#) is the so called the natural frequency of the resonator with it's solution been depicted in the [Figure 2.5](#) above.

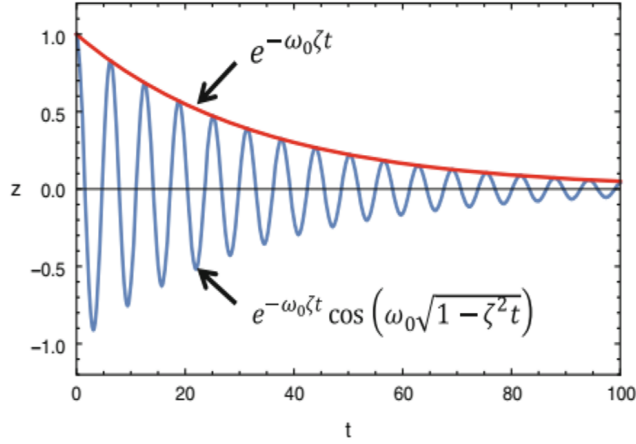


Figure 2.5: A figure illustrating Equation 2.44 the $z_o=1, \Omega = 1$ and $\zeta = 0.03$ from [34].

2.4.2 Driven Damped Resonator

The solution associated with the Equation 2.12 is the sum of the transient solution of the homogeneous differential equation as we saw in Equation 2.36. In reality the specific steady solution that we know is given by:

$$Z(t) = Z_o \exp^{i\omega t} \quad (2.46)$$

In principle the the Z_o is the amplitude associated with the resonator. If the Equation 2.46 is inseted into Equation 2.36 we are able to generate the expression illustrated in the Equation 2.47.

$$Z_o = \frac{F_o/m}{(\Omega^2 - \omega^2) + 2i\zeta\Omega\omega} \quad (2.47)$$

The corresponding phase of the resonator using the lumped element model is expressed as Equation 2.48

$$\arg(Z_o) = \gamma = \tan^{-1} \left[\frac{2\zeta\Omega\omega}{\omega^2 - \Omega^2} \right] \quad (2.48)$$

The real specific steady solution then takes the form as expressed in Equation 2.49

$$Z(t) = \frac{F_o/m}{(\Omega^2 - \omega^2) + 2i\zeta\Omega\omega} \text{Cos}(\omega t + \psi) \quad (2.49)$$

The above amplitude and phase can be expressed in terms of the relative frequency $\frac{\omega}{\Omega}$. This means that we can express Equation 2.49 as Equation 2.50.

$$Z_o = \frac{F_o/m}{\left[\left(1 - \left(\frac{\omega}{\Omega} \right)^2 \right)^2 + \left(4\zeta^2 \left(\frac{\omega}{\Omega} \right)^2 \right) \right]} \quad (2.50)$$

Where $\frac{F_o}{M}$ represents the static deflection with the dynamic amplification or gain been expressed as:

$$\delta z_o = \frac{1}{\left[\left(1 - \left(\frac{\omega}{\Omega} \right)^2 \right)^2 + \left(4\zeta^2 \left(\frac{\omega}{\Omega} \right)^2 \right) \right]} \quad (2.51)$$

One important way by which our mechanical resonator is actuated is by shaking it base by means of a piezoelectric shaker, under this condition the relative amplitude is expressed as shown in Equation 2.52.

$$\delta z_o = \frac{\left(\frac{\omega}{\Omega} \right)}{\left[\left(1 - \left(\frac{\omega}{\Omega} \right)^2 \right)^2 + \left(4\zeta^2 \left(\frac{\omega}{\Omega} \right)^2 \right) \right]} \quad (2.52)$$

The piezoelectric shaker have an associated phase response is given as shown [Equation 2.53](#)

$$\arg(Z_o) = \gamma = \tan^{-1} \left[\frac{2\zeta \left(\frac{\omega}{\Omega} \right)}{1 - \left(\frac{\omega}{\Omega} \right)^2} \right] \quad (2.53)$$

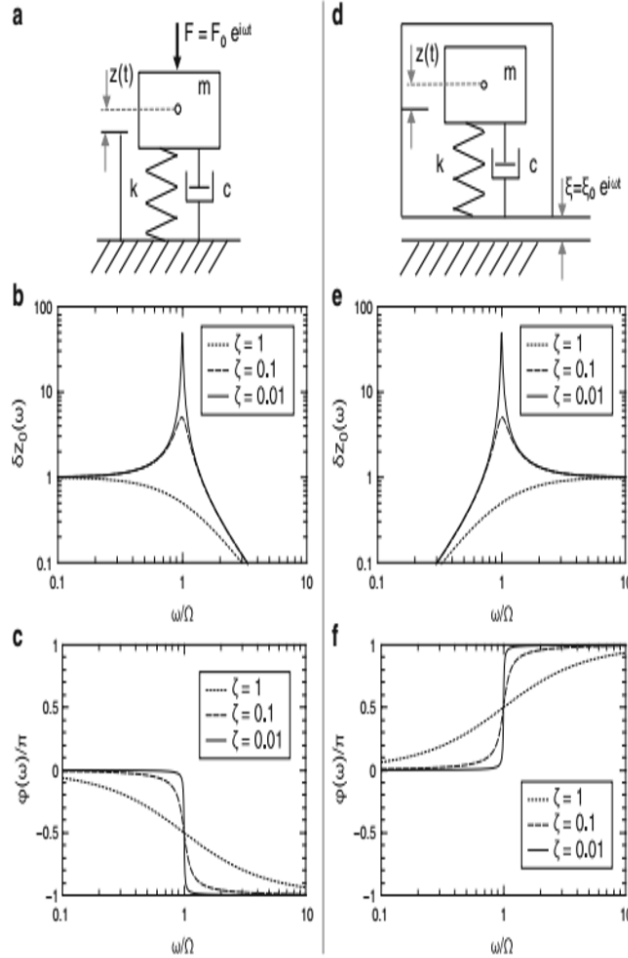


Figure 2.6: Driven damped vibration of a lumped system schematic drawing of a resonator **A**. Driven by force [Equation 2.52](#) **D**. Driven by an external vibration. **B**. and **E**. show the respective relative amplitude response [34].

2.5 Quality Factor

2.5.1 Quality Factor

A key characteristic parameter of resonator is the quality factor. The Q-factor is defined as the ratio of the energy stored to the energy loss during one cycle at resonance.

$$Q = 2\pi \frac{W_s}{W_d} \quad (2.54)$$

Where W_s is the energy stored. W_d is the energy loss. In short the Q- factor defines the rate at which the resonator dissipate energy. The quality factor can also be calculated from the amplitude - frequency spectrum as:

$$Q = \frac{f_o}{\Delta f_o} \quad (2.55)$$

Where f_o is the resonance frequency whiles the Δf_o represents the frequency bandwidth at 3dB amplitude point as shown in [Figure 2.7](#). The quality factor in essence is very important because it determines

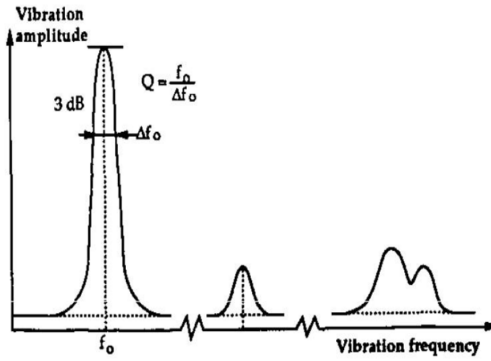


Figure 2.7: Quality factor extracted from the amplitude frequency spectrum of a mechanical resonator [7].

the sharpness of the resonance frequency peak. A high quality factor is desired for application of mechanical resonators. The quality factor of a resonator is the sum of dissipative mechanisms. This means that the energy can be loss to the environment(gas or liquids), through clamping and finally through dissipative mechanism that are intrinsic to the resonator. Operating the resonator in vacuum can eliminates the medium interaction losses while a good optimized design can also eliminates the energy losses through clamping in the form of elastic waves. This leaves us with the intrinsic losses as the the limiting mechanism of the quality factor. Even though this intrinsic losses can be reduced by lowering the operating temperature. The important observation that was made with this Figure 2.8 was that the

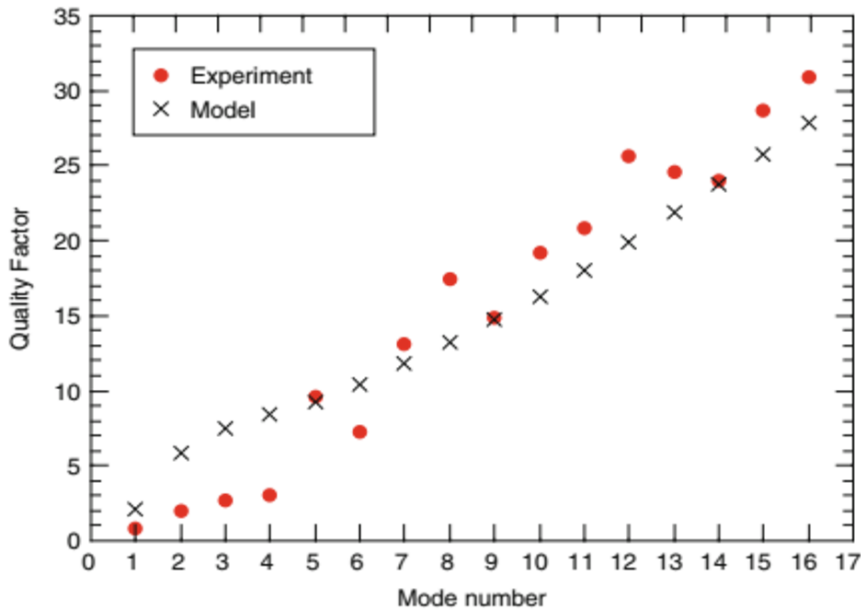


Figure 2.8: A quality factor plotted against the number of mode of a cantilever [34].

quality factor associated with the fundamental was approximately unity. This was the situation where the system was absolutely close to been over-damped. This was the case where the cantilever was immersed in a viscous fluid. Thereafter we could observe that the quality factor increases rapidly for an increase in the flexural mode. The observed trend and patterned by the experiment is well observed in the theoretical model.

2.5.2 Responsivity

A change in mass, temperature or applied force can cause a response in a micro-resonator. This response can either be a change in frequency or vibrational amplitude. The responsivity of a micro-resonator is a

linear slope of the response to a particular stimulant. In case of a sensor application, the *responsivity* to the input parameter(mass) to be measured should be maximal. However,the responsivity to other inputs, such as a change in ambient temperature, should be minimal in order not to cause an unwanted cross-response. The rational to develop micro and nano-mechanical resonators is to achieve unique sensors with exceptional sensitivities [34]. Is the slope of a sensor's output as a function of the input parameter to be measured. If we assume that we are applying the small mass approximation. This assumption

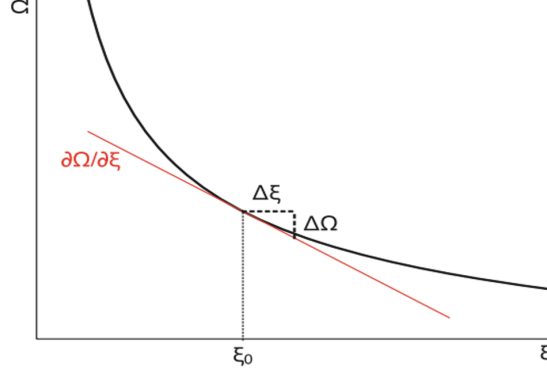


Figure 2.9: Eigenfrequency Ω of linear resonator as a function of arbitrary input parameter ε . The red line represents the slope at ε_o which is the responsivity \mathfrak{R} . [34].

will imply that the change of the parameter to be measured is small and can thus be linearize to obtain Equation 2.56.

$$\mathfrak{R} \approx \frac{\Delta\Omega}{\Delta\varepsilon} \quad (2.56)$$

The sensitivity or the smallest detectable values of the parameter $\Delta\varepsilon$ is approximatly given by Equation 2.57

$$\Delta\varepsilon \approx \mathfrak{R}^{-1} * \Delta\Omega \quad (2.57)$$

Where $\Delta\Omega_{min}$ is the minimum detectable resonance frequency change. The frequency resolution and the $\Delta\Omega_{min}$ associated with the noise of the system could be estimated. Most often the frequency resolution is expressed relative to the resonance frequency as shown in Equation 2.58.

$$\delta\Omega_{min} = \frac{\Delta\Omega}{\Omega(\varepsilon_o)} \quad (2.58)$$

The $\delta\Omega_{min}$ is usually expressed as either part per million(ppm) or part per billion (ppb). In that case we usually expressed the relative responsivity $\delta\mathfrak{R}$ as shown in Equation 2.59

$$\delta\mathfrak{R} = \frac{\mathfrak{R}}{\Omega(\varepsilon)} \quad (2.59)$$

The sensitivity is given as shown in Equation 2.60 :

$$\delta\varepsilon_{min} = \delta\mathfrak{R}^{-1} * \delta\Omega_{min} \quad (2.60)$$

2.5.3 Allan Variance

Allan variance is defined as one half of the time average of the squares of the differences between successive readings of the frequency deviation sampled over the sampling period. The Allan variance depends on the time period used between samples: therefore it is a function of the sample period, commonly denoted as τ (integration time), likewise the distribution being measured, and is displayed as a graph rather than a single number. A low Allan variance is a characteristic of a clock with good stability over the measured period.The Allan variance has become a metric for the frequency noise of the sensors. It is named after it's inventor David W. Allan, the allan variance can apply to any magnitude and it is given by:

$$\begin{aligned} \sigma_y^2(\tau) &= \frac{1}{2} * \langle (\Delta_y)^2 \rangle, \\ \sigma_y^2(\tau) &= \frac{1}{2(N+1)} \left[\sum_{i=1}^N (Y_{i+1,\tau} - Y_{i,\tau})^2 \right]. \end{aligned} \quad (2.61)$$

It can be understood that the Y_i is given by:

$$Y_{i,\tau} = \frac{1}{\tau} \int_{i-1,\tau}^{i,\tau} Y(t) dt \quad (2.62)$$

Allan variance is best known to be expressed in the time domain but it is very important to understand that, in addition to been expressed in time it can also be expressed in the frequency domain. The consequence of the different different kind of noise that affect the resonator is shown in Figure 2.10. In Figure 2.10 we are able to see the allan deviation plot as a function of the integration time τ . The black line shows the overall allan deviation which is affected by three of three different kind of noise. The first is the thermomechanical noise or white noise which is know to be inversely proportional to the integration time ($\tau^{-1/2}$). The second is the flicking or ($\frac{1}{f}$) noise which gives a flat contribution across the integration time. This flicking noise cannot be improved by averaging over a long integration time (τ). Finally the thermal drift noise is seen to show a square root relationship with the integration time ($\tau^{1/2}$) it is the pink line. The most important part of this allan variance is the minimum which provide us the $\delta\Omega_{min}$ as shown Equation 2.58 which is needed in order to compute the minimum detectable mass. The minimum noise can be found in this case is at an integration time of 2 s, but this does not necessarily mean that the $\tau = 2$ s will be the most appropriate operation point. It is known that this minimum might be the one needs to compromise resolution in favor of speed in the measurement. The allan variance or

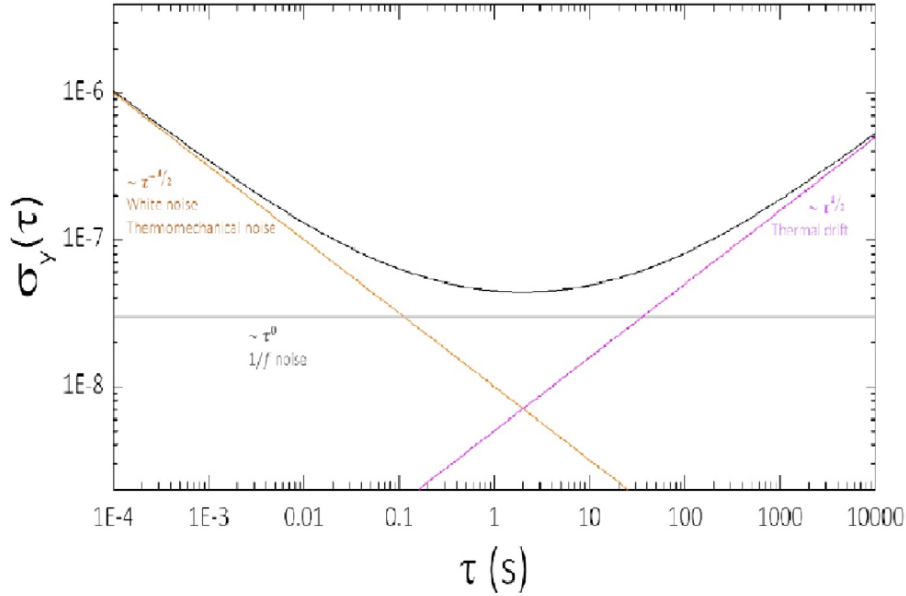


Figure 2.10: The different noise regime of the allan deviation [34].

deviation inherently provide a measure of the behavior of the variability of the quantity as it is averaged over the different measurement time period. This allows the allan variation to differentiate and directly quantify and simply different between the different type of signal variation. The statistical standard deviation does not provide a direct way to distinguish the different types of noise.

Chapter 3

Device Fabrication

3.1 Femtosecond Laser Microstructuring

In the last decades, the suspended microchannel resonators have had a huge impact in the field of biosensing. In fact, these devices show impressive mass resolution (up to 10^{-15} g), which is suitable to study single cell, bacteria and micro or nanoparticles. Unfortunately, one of the main drawback is represented by the complex and expensive fabrication process needed to realize the buried channel, which generally requires multilayer processing. The femtosecond laser writing represents an alternative approach for the suspended microchannel resonators fabrication. In fact, this technique shows some unique advantages, which allow to overcome the limitations described above. First of all it is a maskless technique, which allows to define the SMRs pattern in a single step, without the standard clean room facilities. Second, it can be considered as a 3D technique, thanks to the possibility to define buried channels at variable depths inside the glass. Due to these characteristics, the femtosecond laser microstructuring has emerged as a powerful fabrication tool for different types of lab on chip devices. The femtosecond laser microstructuring also offers the ability to have the modification of the exposed substrate, like the change of the refractive index in a micrometric sized volume [25]. This technique has been widely exploited for the creation of waveguides as shown in Figure 3.1 allowing for a single step 3D fabrication of optical devices.

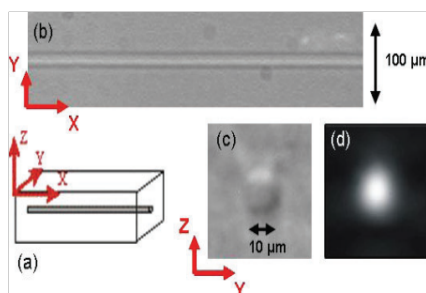


Figure 3.1: The femtosecond laser microstructuring applied in the fabrication of waveguide. With the refractive index contrast between the waveguide and the pristine glass is about $\Delta n = 1.0 \times 10^{-3}$ [25].

The second characteristic of this technique is that the modification induced by the laser irradiation can directly modify the chemical properties of the substrate. In particular for the fused silica, the exposed pattern can be micro-structured applying an appropriate chemical etching technique. The technique which possesses the above characteristics is commonly known as the FLICE, which stands for the Femtosecond Laser Irradiation followed by Chemical Etching. This technique represents a suitable approach for the fabrication of microfluidic devices with embedded channels [25]. Many microfluidic chips are known to be implemented on lab on chip detection systems [33]. In fact, the femtosecond laser writing allows to obtain complex patterns compatible with this application. An important aspect of all femtosecond laser microstructuring is based on the small spot size of the laser. This by logical extension means that during the fabrication the modifications are limited to that specific focal volume of the writing beam. This is an important characteristic that defines the minimum dimensions of the features that can be obtained with this approach.

3.2 Fundamental Physical Mechanism Of Femtosecond Laser Microfluidic Fabrication

In order to understand the physical phenomenon of femtosecond laser pulse, it is important to first analyze the absorption processes of intense pulse. According to Marcinkevicius [23] the first stage deals with a dielectric material that have an energy gap greater than the laser photon's energy. From the semiconductor perspective this is equivalent to the photon energy below the gap of the semiconductor physics. The second stage is that in which there is a nonlinear absorption through the interband transition from the valence band to the conduction band. Even though this is true it is known that at high intensity absorption can take place through non-linear phenomenon like multi-photon absorption, tunneling ionization and avalanche ionization [25].

3.2.1 Non-Linear Mechanism

The *Multi photon Ionization* involves simultaneous absorption of m-photon such that $m h \nu > E_g$. The m-photon having energy greater than the energy gap will result in multiple photon absorption as shown in Figure 3.2a. The multiphoton ionization is applied in the well known technique called the Matrix Assisted Laser Desorption Ionization(MALDI) technique [4]. This MALDI technique is used for the mass spectral investigation of large molecules with low volatility.

The *tunneling ionization* occurs when the high electric field of the laser pulse lowers the coulombic potential of the conduction band as shown in Figure 3.2b. This occurs in such a way that there can be tunneling of the free electron from the valence band to the conduction band.

Avalanche ionization: In order to understand the avalanche ionization process, let us assume that we have a free electron at the bottom of the conduction band. When this electron is exposed to an intense light field, the electron accelerates acquiring a kinetic energy. When the total energy exceeds the conduction band minimum by more than the bandgap energy, it can ionize another electron from the valence band to the conduction band resulting in two electrons near the conduction band minimum. These two electrons can be accelerated by the electric field which will eventually results in the generation of free electrons at the minimum of the conduction band in an exponential manner. This process is called the avalanche ionization process as shown in Figure 3.2c.

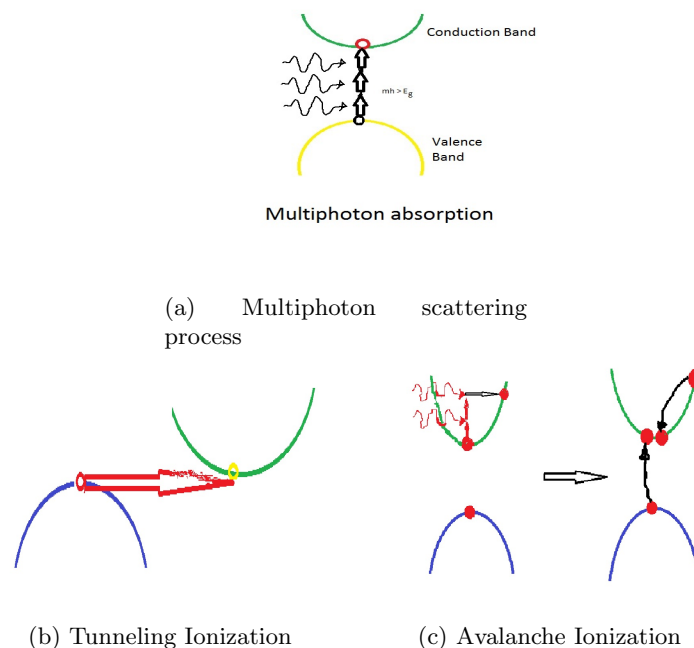


Figure 3.2: A figure illustrating multiphoton scattering, tunneling ionization and the avalanche ionization

3.3 Non Linear Absorption Pulses

The non-linear absorption mechanism can be classified as either a long or short non linear absorption pulse.

Long Non Linear Absorption pulses: This is a kind of non-linear absorption pulse with a duration of multiple picoseconds to nanosecond. When the material is exposed to a long pulse the peak intensity becomes too low to allow multiphoton ionization and tunneling ionization to occur even if the total pulse energy might be high [2]. This implies that for a long pulse laser only avalanche ionization can occur as a nonlinear absorption phenomenon. The number of carriers involved in an avalanche ionization is large thus the long non-linear absorption pulses which have large fluctuation making the absorption process very *erratic* and *poorly reproducible* [25].

Short Non Linear Absorption pulses: This is a non-linear absorption with a duration of sub-picoseconds. When the material is illuminated with a short laser pulse, the high peak intensity makes the multiphoton and tunneling ionization becomes the most significant non linear absorption phenomenon. When the intensities exceeds a given threshold some free electrons are generated in a focal volume by these mechanisms [14]. The electrons that are generated in the focal volume acts as a seed with a fully deterministic behavior. This short laser pulse is in contrast to the avalanche ionization process which is known to increase the number of free electrons in a dielectric material which are erratic and poorly reproducible. The avalanche ionization is known to increase the number of electrons until the plasma frequency approaches the laser frequency at which point the material becomes strongly absorbing. Again the short excitation pulse is known to be formed on a timescale much shorter than that necessary for energy transfer to the lattice. It is therefore clear that only high intensity femtosecond pulse is able to depose energy in a controlled and reproducible fashion in a small volume inside the bulk of a transparent material. This only results in a permanent modification if and only if the energy deposition exceeds a certain threshold. According to Osellame [25] the factors that results in the morphological changes are *exposure parameters* (like energy,pulse duration,repitition rate,wavelength and laser fluence) and *material parameters* (like bandgap and thermal conductivity.) The exposure and material parameters are explained in [section 3.4](#).

3.3.1 Modification classes based on laser fluence

There are two modification classes based on the laser fluence according to Gattas publication [16]. The first modification class occurs when the laser fluence is just above the permanent modification threshold. This results mainly in positive and negative refractive index change according to Taylor's publication [27]. This is the concept that is applied in the fabrication of waveguide [25]. The second modification class on the other hand occurs when the laser fluence seem to be high above the permanent modification threshold according to Taylor's publication [27]. This second modification class is used to generates a sub wavelength nanogratings, so far this is observed only in fused silica when it is oriented perpendicular to the writing laser polarization with a period of $\approx \frac{\lambda}{2n}$ where λ is the wavelength of the laser and n been the refractive index of the substrate [35]. The second modification class is used in the first stage of F.L.I.C.E. which was used to generate the microchannel resonator. Pertaining to the refractive index change three mechanism have been proposed to explain the reason why we encounter change in the refractive in the F.L.I.C.E. These proposed mechanism are explained below. The first possible mechanism according to Chan [10] is the color centered formation, which occurs when the femtosecond laser irradiates the fused silica the femtosecond laser produces in the fused silica a significant number of color centers. These color centers absorbs the U.V light which results in the modification of the Kramer-kroenig relationship[35]. The second mechanism is the *Thermally Induced Material Densification*. According to Osellame publication [25] the energy deposited by the laser melts the material in it's focal volume and is followed by a subsequent rapid resolidification dynamics resulting in a density and refractive index variation [11]. It will results in a high density or high refractive index which is structurally frozen in. The third possible mechanism is the *non uniform cooling process*: After the irradiation, the material melts out to a radius where the temperature becomes equal to the melting glass temperature. The molten material within this maximum radius is quickly quenched and thus solidifies into a low-density structure of the glass. The above quenching continuous radially inward as the glass get cooled down. The solidification occurs because there is no free surface that can expand to take up the extra-volume. This results in the material near the focal region been put under pressure and for that matter been forced into a high density phase or a high refractive index at the core of the structure[35].

3.4 Methods for femtosecond microfluidic writing

Pertaining to the femtosecond laser writing it is known that there are two direct writing geometries. These writing geometries are the transversal and longitudinal writing geometry. In the longitudinal writing geometry, the patterns are found to be intrinsically symmetric with its transverse size determined by the focal spot size which is large in diameter. The drawback of the longitudinal geometry is that the length of the pattern is however limited by the focal length of the objective. The second drawback of the longitudinal geometry is that the quality of the patterns is degraded by spherical aberration. The spherical aberration is able to increase the depth of focus inside the glass sample. Pertaining to the transverse geometry, it is also known that the transverse geometry provides a much greater flexibility during the patterns writing of arbitrary length and geometry. The major disadvantage of this transverse writing geometry is that it generates a cross section that is strongly asymmetric in nature. The reason why the transverse geometry generates a strong asymmetric microfluidic cross-section is because the beam that propagates in the perpendicular direction has a beam focal diameter of:

$$\approx 2w_o$$

while the beam focal diameter along the propagation direction is given by the confocal parameter

$$b = \frac{2\pi w_o^2}{\lambda}$$

Where, w_o is the beam width and λ is the wavelength.

Nonlinear absorption will only occur in glass if and only if the exposure parameters are right. This exposure parameter includes having a laser intensity (I) of about

$$I \approx (1 - 5) * 10^{13} \frac{W}{cm^2}.$$

The associated pulse duration is about

$$\tau \approx 100fs.$$

The fluence (F) associated with the laser is about

$$F \approx (1 - 5) \frac{J}{cm^2}.$$

These exposure parameters required to achieve the above fluence depends on the focusing condition. There are two focusing conditions that have been identified the first focusing condition is the **Mild Focusing**: This focusing has a laser's beam waist of about $(1 - 3)\mu m$. The pulse energy is only few $\mu Joules$. It is when these two characteristics are satisfied that we can say that we are having the mild focusing condition. The second focusing condition is the **Extremely Tight Focusing**: The extremely tight focusing occurs when it is known to have half the wavelength of the mild focus and also known to be diffraction limited. The pulse energy is known to be

$$\approx 10nJ.$$

The femtosecond laser writing can be distinguished depending on two pulse periods. They include: A long or short time required for heat to diffuse away from the focal volume. The operating regimes of femtosecond writing are the first regime: *Low Frequency Regime*: Is the regime in which the material modification is produced by an individual pulse. The second regime *High Frequency Regime*: This is the regime in which the material modification is produced by the cumulative pulse effect, since the heat diffusion time out of the absorption volume in glass is

$$\approx 1\mu s.$$

This means that the transition between the two regimes takes place at a frequency around 1MHz [12].

3.4.1 Femtosecond Writing Set Up

The Figure 3.3 illustrates the setup for the femtosecond laser writing. This same system is used for the irradiation step in the FLICE process. The functions of the components are illustrated below: The *Variable Attenuator*: Is the component that is mainly used to reduce the power level of an optical signal. The variable attenuator achieves this power level reduction by using a neutral density filter and the associated advantages of using a variable attenuator are that the wavelength and optical modes become

insensitive with the dynamic range. The second component under consideration is the *Mechanical Shutter*: The mechanical shutter blocks the laser radiation from being transmitted when the shutter is closed. The shutter opens to allow the laser to be transmitted. The third component is the *Second Harmonic Generator Module*: This module undergoes a nonlinear optical process by two photons with the same frequency. This will eventually be able to interact with the material in order to generate a new photon with twice the energy of the initial energy. The SHG is also called the frequency doubling. The fourth component is called *Polarization Controller*: This is an optical device which allows one to modify the polarization state of light. In this case it has automatic feedback and its task is with the act of transforming the arbitrary polarization into a well known fixed polarization. In order to increase the refractive index contrast we have to use a completely different irradiation parameter. In particular it has been found out that the waveguide writing with a repetition rate ($\approx 1\text{MHz}$) and with a beam shaping optics can provide a significant increase in the refractive index [20]. The article also states that the use of the second harmonic improves the waveguide homogeneity. This is because the second harmonic module reduces the propagation losses due to the increase of the photon energy. In our quest to increase the refractive index contrast, it is very important to be mindful of the fact that the increase in refractive index contrast can be achieved at the expense of damaging the glass.

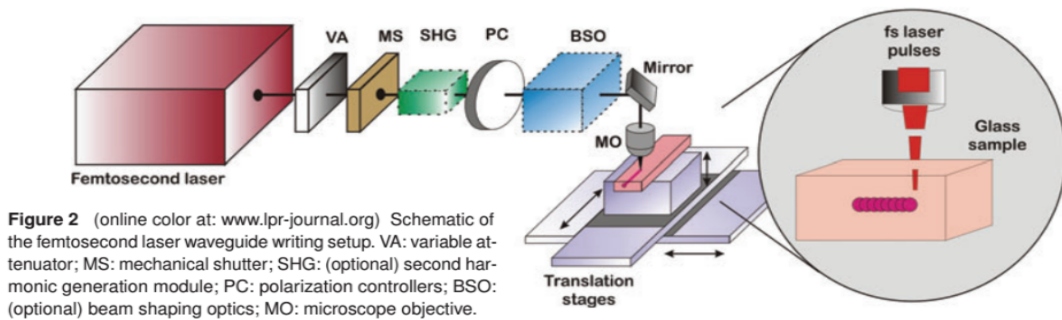


Figure 3.3: A figure illustrating setup of the femtosecond laser writing from [25] article.

According to Osellame [25] only two materials have been successfully used for the generation of microfluidic channel fabrication. These materials are *fused silica* and *Foturan* but it is much desirable to concentrate on the generation of microfluidic channel in fused silica. The characteristics that makes fused silica an excellent material for microfluidic is the increased etching rate with HF or KOH after being irradiated with femtosecond laser. The high etching rate of the modified fused silica is due to two mechanisms. The first mechanism has to do with the decrease of the Si-O-Si bond angle which is induced by the hydrostatic pressure [21]. This explanation is particularly suitable for low intensity regime which corresponds to the formation of microfluidic channels. With this condition the etching rate has been shown to be proportional to the increase of the refractive index [26]. The second mechanism however is the mechanism which is active for high intensity irradiation and gives rise to a high etching selectivity through the self-ordered nanocracks formation. This self-ordered nanocrack is perpendicular to the polarization direction and act as directing structure for the channel formation during the chemical etching bath.

3.5 Fabricated Suspended Microchannel Resonator

There are several reasons why we decided to fabricate our microchannels in fused silica. The first reason was that the fused silica have a low coefficient of thermal expansion which is around $3.0 \times 10^{-6} C^{-1}$. The logical implication of this is that glass is thermal resistant to thermal shock and less subjected to thermal stress. The second reason why we used silica glass as material to fabricate the microchannel was because the silica glass can be bonded to the PDMS (Polydimethylsiloxane) which was perceived as a material for the connectors. Finally the glass is known to be chemically inert and stable in time. It is hydrophilic, nonporous and optically clear. The fused silica as a substrate material gives an added advantage of being optically transparent up to the UV range with low background fluorescence.

The suspended micro channel resonators that were fabricated using the FLICE technique optimized in collaboration with FEMTOprint[®] illustrated in the Figure 3.4. This consists of the modification of a 0.5 mm thick fused silica slice using a 1030 nm femtosecond pulsed laser (Ytterbium fiber). The exposed

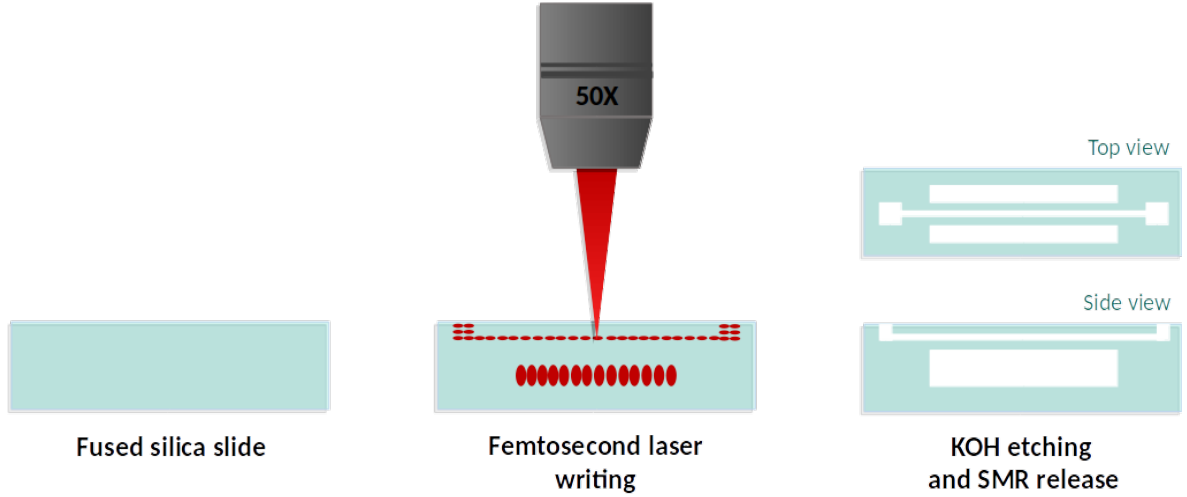


Figure 3.4: A figure illustrating the FLICE technique which was optimized in collaboration with the FEMTOprint[®]

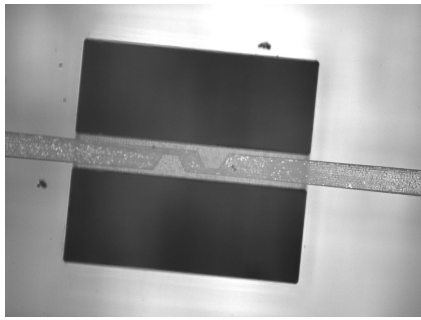
focal volume to the laser was around 523 m³, obtained working with a 50x objective with 0.65 NA. Then the glass slide was kept in a high concentrated KOH etching bath for 8h. The SMRs were designed considering different geometries, in particular four different type of SMRs were fabricated as shown in [Figure 3.5b](#), [Figure 3.5d](#), [Figure 3.5f](#) and [Figure 3.5h](#). Each of them shows a constriction of the channel path in the middle of the suspended beam which are also shown in [Figure 3.5a](#), [Figure 3.5c](#), [Figure 3.5e](#) and [Figure 3.5g](#). This constrictions have been taken into account to evaluate the possibility to slow down the velocity of the fluid in the central part of the resonator, which is characterized by the maximum amplitude of displacement at the resonance frequency of the SMR, increasing the permanence time of the fluid in that region. The first micro resonator that was fabricated is illustrated in [Figure 3.5a](#). The Z constriction is just an insertion of two solid trapezium within the channel. The second resonator that was analyzed is shown in [Figure 3.5c](#). The constriction is very similar to the previous resonator in the sense that it also having the two trapezium solid that have the presence of the 10x10x35 rectangular solid located within them as shown in [Figure 3.5d](#). The third micro resonator under consideration which is illustrated in [Figure 3.5e](#), shows the constriction which is X shaped and can be represented as two solid trapezium adjacent to one each other as shown in [Figure 3.5f](#). The main reason why the constriction was introduced into the design of the micro channel resonator was to aid in slowing down the nanoparticles motion through the channel. In our quest to simulate and characterize the micro-channel resonator it was important to understand the dimensions of the fabricated channel [Figure 3.5](#) and to evaluate the theoretical volume occupied by the constriction as shown in [Table 3.1](#).

	500-55-Z	500-55-Z0	750-30-XX	500-55-X
Length [μm]	500	500	750	500
Outer Width [μm]	75	75	75	75
Inner Width [μm]	55	55	30	55
Volume Of Constriction [pm^3]	0.105	0.108	0.036	0.0405
Volume Outer Plate [pm^3]	1.6875	1.6875	2.53125	1.6875
Volume Of Hallow Plate [pm^3]	0.825	0.825	0.675	0.825
Volume Accessible To Fluid [pm^3]	0.72	0.717	0.639	0.7845
Mass Of The Resonator [μg]	2.1314	2.1380	4.1687	1.9871

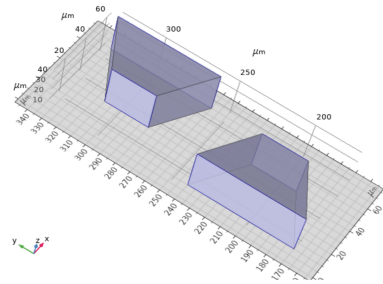
Table 3.1: A table illustrating the summary of the geometrical characteristics associated with the different micro resonator.

3.6 Process Flow For PDMS Integration

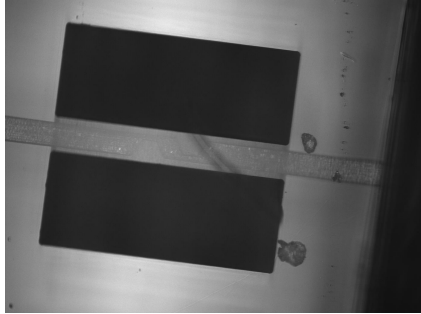
In this section the idea is to explain the process flow necessary in order to integrate Polydimethylsiloxane with the suspended micro channel resonator. Plasma oxygen bonding was used to integrate the suspended micro channel resonator with the Polydimethylsiloxane. The motive for this



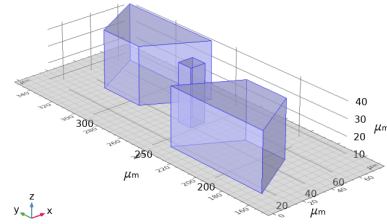
(a) The 500-55-Z resonator



(b) The Z constriction In 3D

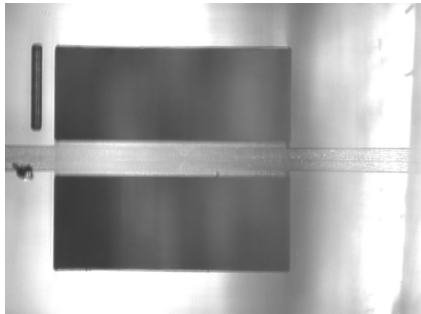


(c) The 500-55-Z0 resonator

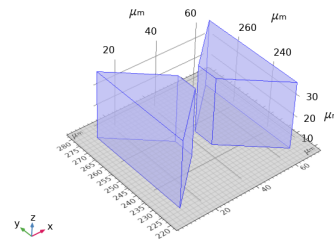


(1).png

(d) The Z0 constriction In 3D

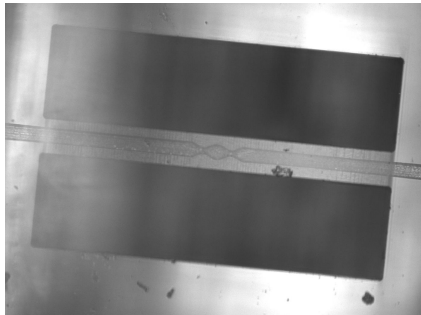


(e) The 500-55-X resonator

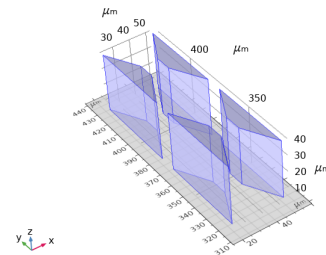


(1).png

(f) The X constriction In 3D



(g) The 750-30-XX resonator



(1).png

(h) The XX constriction In 3D

Figure 3.5: A figure illustrating the images and the schematics associated with different constriction of the suspended micro channel resonators.

integration was to aid the flow the liquids through the micro fluidic channel.

3.6.1 Silicon Mold Process Flow

The PDMS microfluidic channel was realized by following these different steps as illustrated in [Figure 3.7](#). The first step was coating the silicon wafer with a negative photoresist. This negative photoresist is the kind of resist in which the portion of the resist that becomes exposed to light remains after developments . The second step deals with the transferring of the fluidic patterns by means of the laser direct writing. The photoresist development only results in the removal of the unexposed photoresist. In the third step there is the dry etching of the unprotected silicon surface. This dry etching process is extremely important because it allows for the correct transfer of the microfluidic patterns onto the silicon substrate. The final step deals with the stripping the photoresist and the passivation of the silicon surface

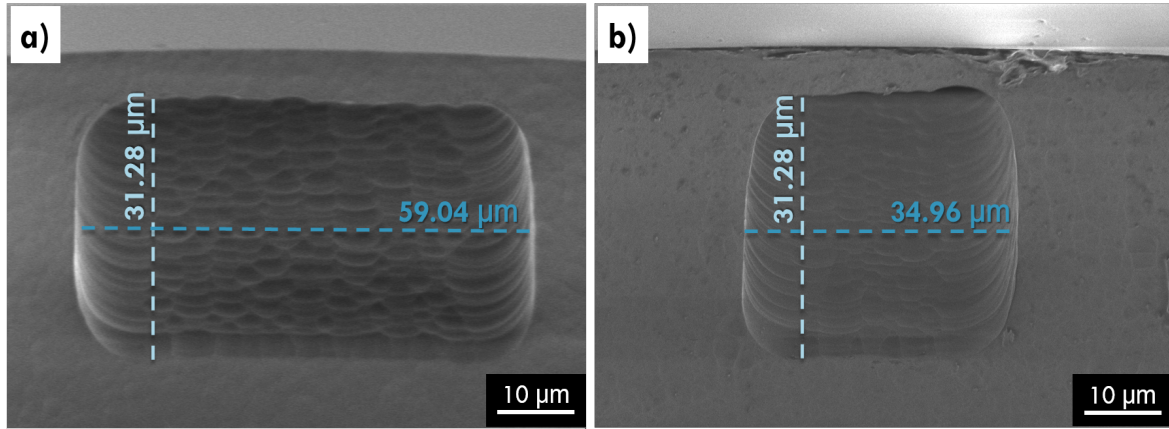


Figure 3.6: A figure showing the SEM image for A. $55\mu\text{m}$ B. $30\mu\text{m}$ channel micro-channel resonator

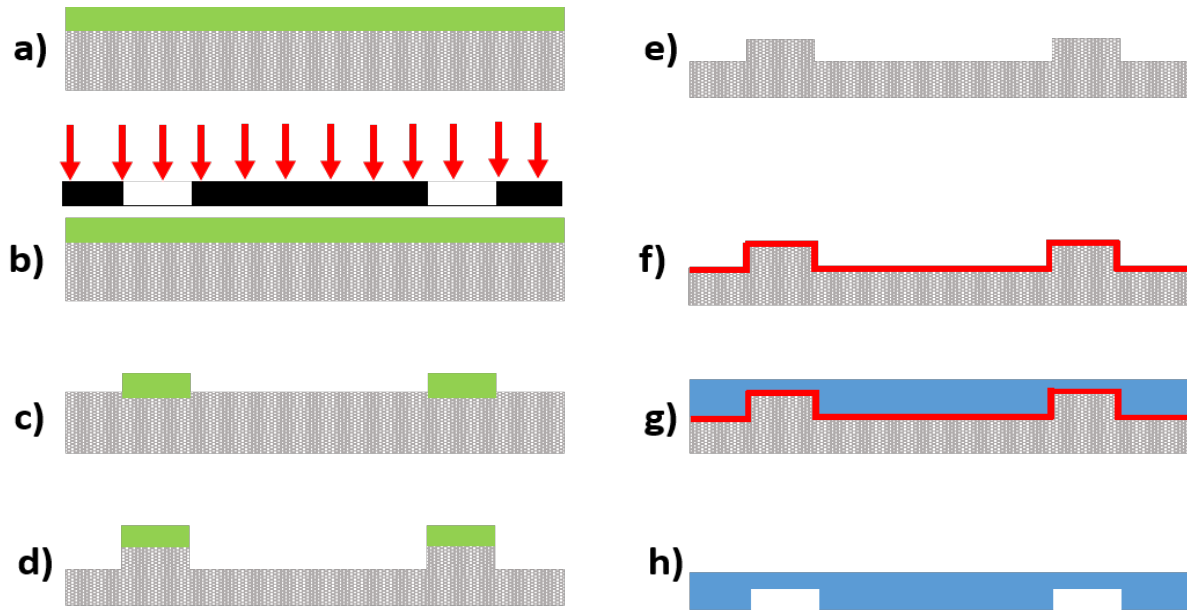


Figure 3.7: A figure showing the silicon mold process **A.** Deposition of the negative photoresist **B.** Exposure **C.** Development **D.** Dry Etching **E.** Stripping **F.** Passivation with PFOT **G.** PDMS deposition **H.** PDMS Mold

with Perfluorodecyltrichlorosilane (PFOTS). The Perfluorodecyltrichlorosilane(PFOTS) deposition was performed overnight at room temperature. The advantage of this passivation is to ensure that the PDMS demold after polymerization as shown in [Figure 3.7](#).

3.6.2 PDMS Glass Bonding Process Flow

The PDMS(Sylgard 184) was prepared by mixing the polymer and the cross-linking agent in a ratio of 10:1. The mixture was then poured unto the above silicon mold for a duration of 2 hours at a temperature of 60°C . The PDMS mold was formed and cutting the single PDMS blocks which is known to contain the microfluidic patterns. The oxygen plasma bonding was undertaken to enhance the PDMS bonding with that of the glass. The bonding did occur at a power of 20 Watt, a duration of 40 seconds and a flow rate of 30 standard cubic centimeters per minutes of the oxygen gas. Careful attention was given to the alignment of the microfluidic patterns within the PDMS and the SMR within the glass. Contact and heating treatment was performed at 80°C for a duration of 10 minutes was performed. The [Figure 3.8](#) is showing the final product after the bonding process which is linked to the connectors which will finally allow the flow of the liquids through the micro channel resonator.

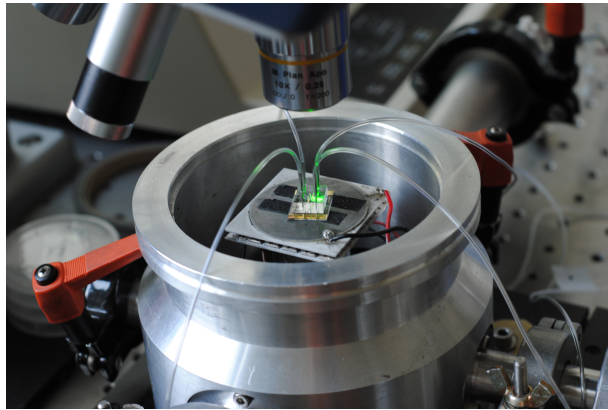


Figure 3.8: A figure showing the final product after the bonding

Chapter 4

Methodology

4.1 Simulation Using Multiphysics Comsol

The workflow for simulating the mechanical structures in comsol involves seven steps which will be explained in detailed with respect to 500-55-Z micro channel structure. The first stage deals with setting up the model environment. The second stage involves the ability of creating the geometrical object. The third stage regards the identification of the material properties. The fourth stage deals with the definition of the physical boundary conditions. The fifth stage that follows explains the procedure of generating the mesh and the sixth stage involves finally running the simulation. Thereafter, there is the seventh stage which takes into account the possibility of performing the post-processing of the obtained data.

4.1.1 Sitting Up The Model Environment

Open the multiphysics comsol and select the click on the wizard. Thereafter there is the possibility to selection the dimension of the structure that is under consideration. In our study the structure was a 3 dimensional structure so '3D' structure was selected. The next task is to deal with the physics that guides our simulation. In our case the relevant physics was the 'Solid Mechanics'. The 'Add' button was selected in order to add the relevant physics. The next line which needed to be considered was to introduce the study which was needed in order to understand the physics. This could be stationary, time dependent study or eigenfrequency study. In our case we needed study the eigen frequency thus the 'Eigenfrequency' study was selected and illustrated in [Equation 5.1](#).

$$\begin{aligned}\Omega = \omega &= \beta_n^2 C_E \sqrt{\frac{I_y}{A}}., \\ \Omega = \omega &= \beta_n^2 \sqrt{\frac{EAh^3}{12\rho Ah}}. \\ \Omega = \omega &= \beta_n^2 \sqrt{\frac{Eh^3}{12} \frac{1}{\rho h}}.\end{aligned}\tag{4.1}$$

4.1.2 Creating Geometrical Object

In the geometry section of the command just click it. Change the length unit to ' μm .' as shown. Go to the model builder section called the 'Global definition' and set the parameter as shown in [Table 4.1](#). Using the parameters Beam Length ,Internal Beam Width and the Beam Width. The hollow plate was generated using the boolean and partition function called difference. Finally using the vectors P,Q and B it is possible to generate the constriction within the hollow plate as illustrated in [Table 4.1](#). To conclude the geometry creation of the hallow plate with constriction the 'Build All' button was clicked in order to visualize the geometry.

4.1.3 Material Parameters

This section deals with the definition of the material. This was obtained by going to the model builder section and right clicking on the materials. Select the browse material and finally select silica glass. Click

	Symbol	Number μm
Beam Length	BeamL	500
Internal Beam Width	IBeamW	55
Beam Width	BeamW	75
Internal Beam Height	IBeamH	30
Beam Height	BeamH	45
Center x Co-ordinate	x_0	0
Center y Co-ordinate	y_0	0
Center z Co-ordinate	z_0	0

Table 4.1: A table illustrating the eigen frequency when the 500-55-Z micro resonator was filled liquids using comsol simulation.

on 'Add to component' and finally click on Done. The domains are the component which is known to be made of silica glass and in this case the domain were from 1 to 5. This was the reason why all the domain which is from 1 to 5 were selected. Again at the setting section ensure that the Young's Modulus is 73.1×10^9 Pa whiles the poisson ratio is set to 0.17.

4.1.4 Defining The Physics Boundary Condition

Right click on the 'Mechanical Structure' and select the 'Fix Constraint'. Right click on the 'Fix Constraint 1' and select the domain 2 and 5 manually. The domains 2 and 5 are really interface where there is there was no displacement. Finally the fixed constraint were applied. The procedure explained above was applied mainly because form the theory we had to ensure that the termination of our structure. This is a common process in all finite element analysis just in order to generate a closure for the equations.

4.1.5 Creating The Mesh

In the model builder we have to select the 'mesh1'. Right click on the Mesh1 and ensure that the 'free tetrahedral mesh' is selected. This free tetrahedral mesh will appear in the model builder. Right click on the free tetrahedral and select 'Size'. An element size dialogue box appears at the general physics section you will see 'Predefine'. Select the Extra fine and final click on the 'Build All'. The use of proper mesh allows for accurate analysis, regardless of whether the simulation is done automatically or manually. In order to generate a successful and a marketable product it is extremely important that the meshing is able to generate result which aid in the correct analysis of the product. If your project requires analysis before moving to the next stage of project design, be sure to use a product development professional to help insure the analysis is done accurately and thoroughly for best results.

4.1.6 Simulation

First there is the need clean up the module builder by collapsing many of the taps leaving the 'Study 1'. Select the 'Study 1' Eigenfrequency and a study setting dialogue box appears will appear. In the study setting dialogue box there is the need to set the desired number of eigenfrequencies = 6. The number 6 was chosen mainly because with this number one can be able to see the first,second,third flexural mode as well as the first torsional mode. There is also the need to choose the frequency center which in this case was set to = 0 [MHz]. After parameter setting right click on the Study1 and select the compute in for the multiphysics comsole to start the computation. Pertaining to the simulation in with the liquids. The only difference that was made pertaining to the previous [subsection 4.1.2](#) geometry was that there was no need for the difference boolean and partition function. Two blocks were designed and different material parameters. One was the material parameter of the silica glass as explained in [subsection 4.1.3](#) whiles the other parameter was for the liquid. The same procedure as explained above was performed in the simulation with the fluid was done details of this is shown in [chapter 5](#).

4.2 Polytec Laser Scanning Vibrometer

The polytec laser scanning vibrometer consist of the following three units. They include the electronic units, scanning head unit and laser generation unit.

4.2.1 Electronic Unit

The electronic unit consist of the following components. The first component is the Junction Box: This components is mainly responsible for connection to external signals and triggering signal output. The second component of the electronic unit on the other hand is the Vibrometer Controller: This is the core for the decoding and controlling of the laser interferometer signals. The last component is the Data Management System: This is the component that is running, displaying and storing the measured data of the the PSV software. This data management system like all computers have a monitor for the display of the results.



Figure 4.1: A figure showing the electronic unit of the polytec laser scanning vibrometer

In [Figure 4.1](#) we are able to see the complete electronic units of the polytec scanning vibrometer [\[1\]](#).

4.2.2 Scanning Vibrometer Head Unit

The second unit of the polytec scanning vibrometer is the *scanning vibrometer head unit*. This is a central component of the polytec consist of the following. The interferometer, an inbuilt video camera and a high quality and a highly precision scanning. It is this high precision scanner that allows for the deflection of the laser beam to the objects.

The laser scanning vibrometer operates using the *Doppler effect* for it's non-contact optical characterization. This effects deals with how the frequency of light is slightly changed when the light is scattered from a moving objects. Within the polytech vibrometer we have a high precision interferometer which is able to detect the minute frequency shift because of the backscattered light. This is archived when the interferometer is able to split the light into two main parts. The first part is called the *reference beam* propagate directly into the photo detector as shown in [Figure 4.3](#) in red color.

The second part is called the measurement beam which is made to incident on the object under investigation as shown in green in [Figure 4.3](#).The object under investigation is been actuated by the piezo. Now depending on the velocity and the displacement of the object under investigation a back scattered light whose frequency and phase haved been changed is made to incident on the photo detector. It is extremely important to remember that the characteristic of the moving object is contained in this backscattered light. The superimposition of the backscattered light with the reference beam creates a modulated detector output signal which reveals the Doppler shift in frequency. The signal processing provides the



Figure 4.2: A figure showing the scanning vibrometer of the polytec laser scanning vibrometer

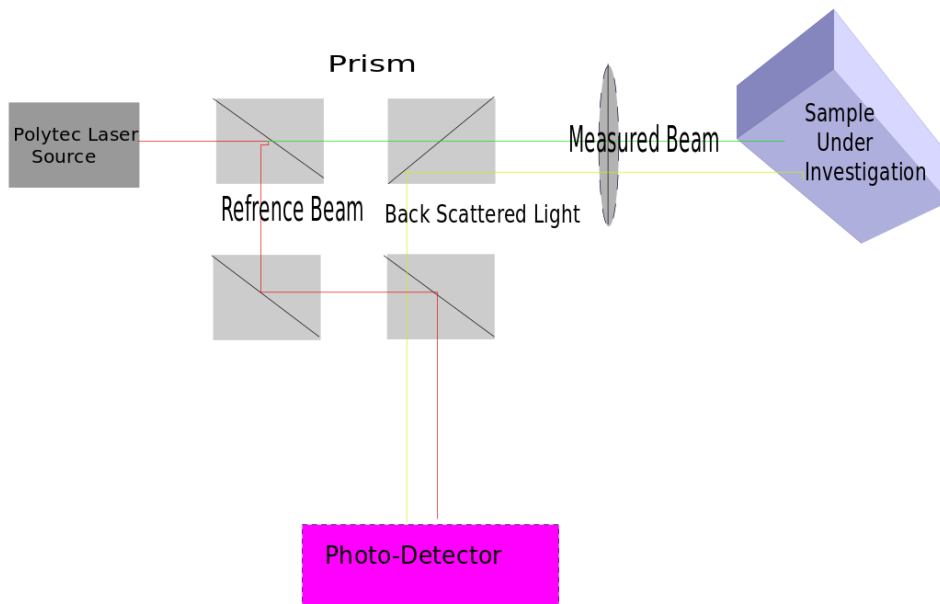


Figure 4.3: A figure showing the polytech scanning vibrometer operation.

- i) Resonance frequency.
- ii) Displacement and the velocity of the test object.

The vibrational motion of the object can truly be characterized as a 3D object by using the poly 3D scanning vibrometer. This provides us with the spatial nature of the motion. The first reason why we need to perform vibrational measurement is that it helps to unravel the critical system dynamics of the test object. The scanning mirrors are able to place the light on a sequential grid. In the end it is able to measure the sequential grid of point on the surface.

The three dimension scanning vibrometer is uniquely able to determine the vector of motion associated with these point. The vibrometer is also able to deliver a real time results that helps us to understand the temporary signature of the material under investigation. The frequency response helps to display the characteristic of the resonator.

4.3 Measurement

4.3.1 Performing Scan Measurement Of S.M.R. In Air

In order to determine the resonance frequency of the micro-resonator in air. The following steps were followed using the latest 3D scan vibrometer in the politecnico nano-micromechanical lab. The loading of the sample was the first thing that was done as shown in [Figure 4.4](#). The glass suspended microchannel resonator was loaded. The objective focus was then adjusted until a clear suspended micro-resonator was seen on the monitor of the electronic unit.

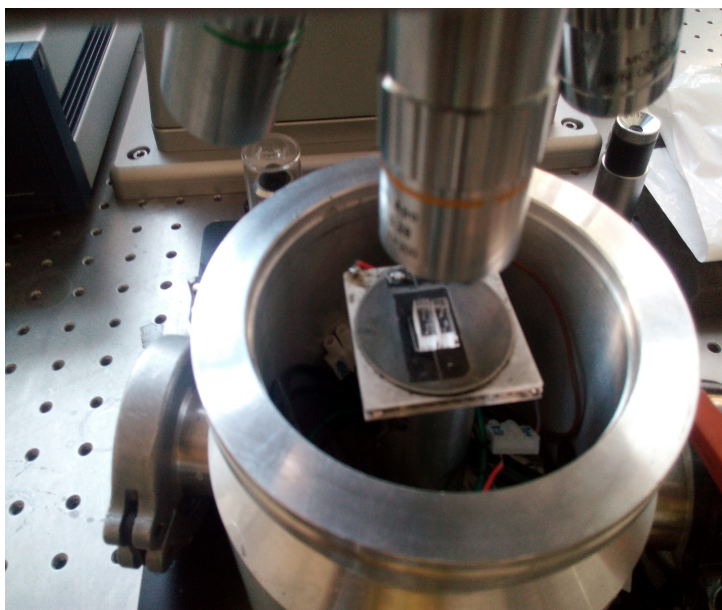


Figure 4.4: A figure showing the loading of the micro channel resonator

The next step was to perform the 3D alignment this was archived by focusing the laser along the suspended microchannel resonator. Drag and click a number of point until a significant amount of point are selected along the bridge and the two fixed ends. Finally by clicking on the 3D alignment command the system gets automatically aligned. Now from the command window click on the define scan point. Click and drag to defined a mesh on the surface of the micro resonator. You can rotate or change the number of point associated with the grid. Now let us go to the A/D settings and thus change the following parameters:

- a) Vibrometer detector.
- b) Reference voltage.

Loading to the micro channel resonator as shown in [Figure 4.5](#). The only difference that exist is that fact that while the resonance frequency is in the continuous mode, The liquid is flushed from one end to another as illustrated in the [Figure 4.5](#) which have one of the tube as inlet whiles the remaining three tubes serve as outlet through which the liquid flows.

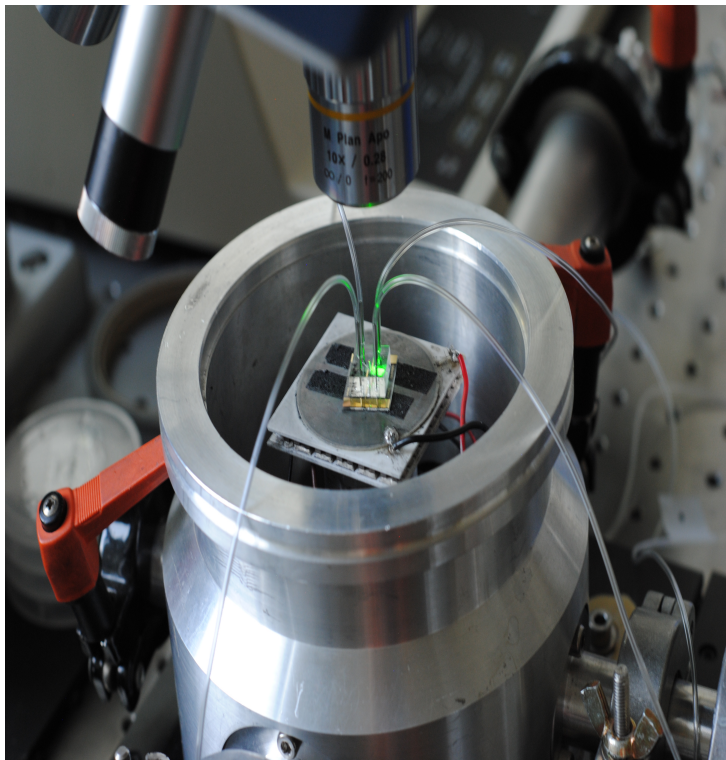


Figure 4.5: A figure showing the loading of the micro channel resonator with the micro tubes for the liquids measurement.

Chapter 5

Results And Discussion

In this section are reported the detailed analysis performed for different SMRs geometries. The sample 500-55-Z, illustrated in Figure 5.1a, has been used as representative sample for which are reported the simulations and the mechanical measurements in extended form. At the end of the chapter is reported the whole comparison between the different analysis and simulations conducted over all the microchannel resonators design.

5.1 Simulation

Before any experimental characterization of the suspended micro-resonator can be made, it was important to simulate the mechanical behavior in order to have an idea about where the eigen-frequencies lies. The simulation also helped us to validate the results obtained from experiment. The resonance frequency was expressed in theory chapter as:

$$\begin{aligned}\Omega = \omega &= \beta_n^2 C_E \sqrt{\frac{I_y}{A}}. \\ \Omega = \omega &= \beta_n^2 \sqrt{\frac{EAh^3}{12\rho Ah}}. \\ \Omega = \omega &= \beta_n^2 \sqrt{\frac{Eh^2}{12} \frac{1}{\rho}}.\end{aligned}\tag{5.1}$$

The above Equation 5.1 is really important because it is the equation that provide the eigenfrequency for the simulation. Considering the fused silica as the material used for the suspended microchannel resonator fabrication, the simulation parameters used were: Poisson ratio equal 0.17, Young's modulus of 73.1GPa and density equal to $2203kgm^{-3}$ For this specific case, the geometric parameters of the suspended micro-resonator were: length $500\ \mu m$, width $75\ \mu m$ and high $45\ \mu m$. Furthermore, the hollow region is characterized by the presence of a constriction in the middle of the suspended beam, for this reason it has been necessary to take into account also the geometric parameter of this feature.

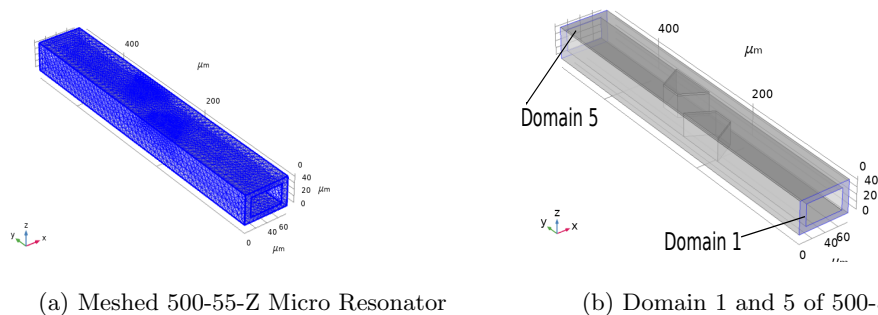


Figure 5.1: A figure illustrating the meshing and the fixed domain 1 and 5 of the 500-55-Z micro resonator.

First of all it has been evaluated the dimension of the buried [Figure 5.1a](#) channel: length 500 μm , width 55 μm and high 30 μm , the constriction has been take into account by creating two solid with trapezoid shape as shown in [Figure 5.2](#). The associated mesh of the 500-55-Z micro resonator was done by applying an extremely fine mesh as shown in [Figure 5.1a](#). In order to simulate the real condition of the beam motion, it has been necessary to fix the boundary conditions. In particular, the domain 1 and domain 5, in other word the clamped ends of the suspended beam has been assumed fixed. [Figure 5.1b](#) has been assumed fixed with displacement equal zero during the oscillation of the beam [\[15\]](#).

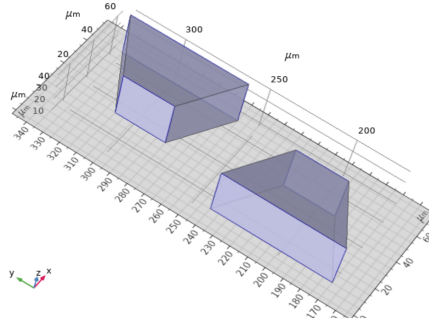


Figure 5.2: A figure illustrating the shape of the constriction of the 500-55-Z Micro Resonator

5.1.1 Simulating 500-55-Z Filled With Air

Once the proper model for the simulations is defined, the eigenfrequency for the first, second and third flexural mode were evaluated and are respectively 1.0334 MHz, 2.6415 MHz and 4.6043 MHz as shown in [Figure 5.3a](#), [Figure 5.3b](#) and [Figure 5.3d](#). Furthermore, with the same approach it has been

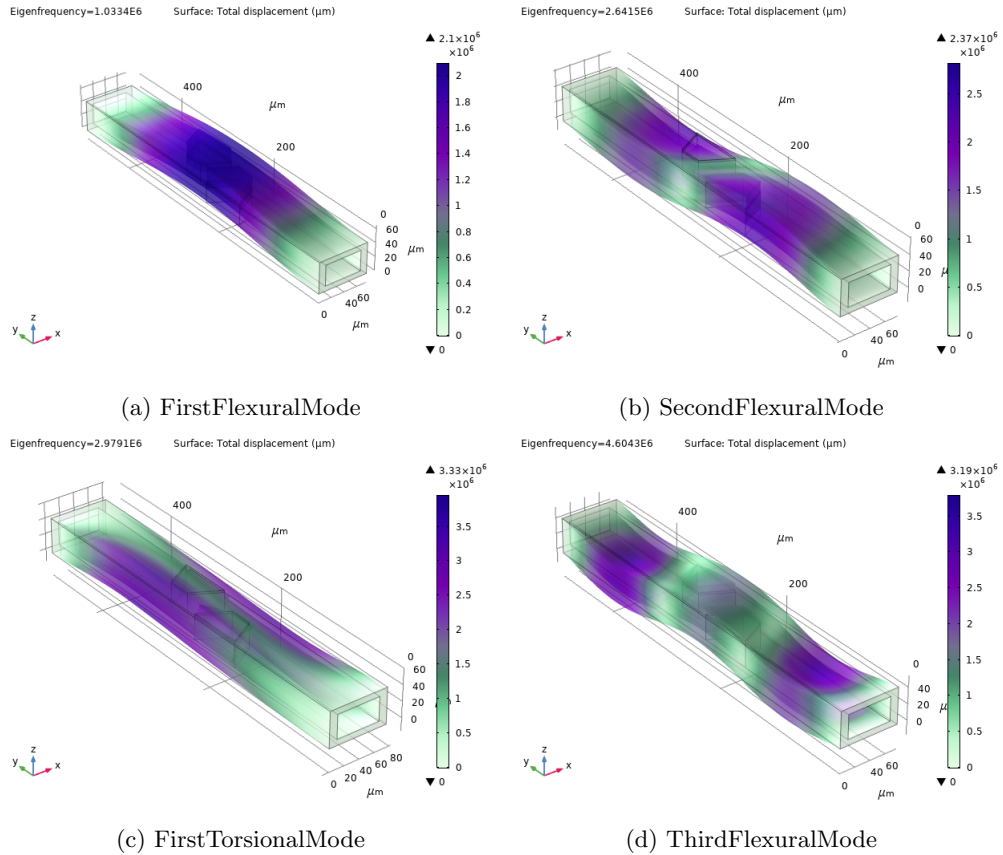


Figure 5.3: A figure illustrating the simulated modes of the 500-55-Z in Air.

possible to simulate also the eigenfrequency associated to the first torsional mode, which is 2.9791 MHz [Figure 5.3c](#). All the simulations were done considering the microchannel resonator filled with Air. This choice was mainly due to the real SMR usage conditions, which foresee the mechanical characterization

in air. In fact, considering the dimensions of the suspended resonator the vacuum environment does not significantly improves the SMR performance as observed in the work of [Calmo et al.](#)

5.1.2 Simulating 500-55-Z Filled With Liquids

After the preliminary simulations about the mechanical behavior of the SMRs, a second set of simulations has been carry out. In particular, it was about evaluating the frequency shift due to the presence of fluid, with different density, within the suspended microchannel resonator. The suspended microchannel resonator simulations were obtained considering the resonator filled with ethanol, water and citric acid (25% water solution). The geometric parameters of the resonator remains the same used for the simulation in air environment. The only difference that was the material parameters for the internal volume, which is the space occupied by the different liquids.

	Eigen Frequency [MHz]	Percentage Change %
Air Filled	1.0334	-
Ethanol Filled	0.9507	8.00
Water Filled	0.94645	8.41
Citric Acid Filled	0.93386	9.63

Table 5.1: A table illustrating the eigen frequency when the 500-55-Z micro resonator was filled liquids using consol simulation.

For this purpose, the empty volume was considered as a bulk rectangle (with the dimensions of the buried channel), and depending on the fluid that should be simulated it has been associated a specific material parameter. The water, for instance, has a Poisson's ratio of 0.46, Young's modulus associated of 3.0 GPa, the dynamic viscosity is equal 8.9×10^{-4} Pa.s and the density at 20 °C is equal to 1000 kg/m^3 . As shown in [Table 5.1](#) the eigenfrequency was found to be 0.9507 MHz when it was filled with ethanol whiles the eigen-frequency was found to be 0.94645 MHz when it was filled with water. When the micro channel resonator 500-55-Z was filled with citric acid the eigen frequency decreased even further to 0.93386 MHz as shown in [Table 5.1](#). One important conclusion that can be made from the simulation point of view was the fact that eigen-frequencies moved to the lowest value when it was filled with citric acid which was followed by water. The highest eigen frequency was found when the micro channel resonator was filled with ethanol. This was in complete agreement with the theoretical equation illustrated in [Equation 5.1](#). The main motivation was based on the fact that the citric acid was the most dense liquid which meant that it must provide the lowest eigen frequency. The highest eigen frequency from the liquid measurement perspective was found in ethanol since it was the less dense liquid under consideration. The same procedures have been used to simulate the mechanical behavior for the other resonators, which will be tabulated and discussed in the [subsection 5.4.1](#).

5.2 Mechanical Characterization

Considering the results obtained from the simulations the first, second, third flexural mode and the first torsional mode would be located at a frequency from 0.5 MHz to 5 MHz. [Table 5.2](#) are reported the experimental frequencies for the first, second, third flexural mode and for the first torsional mode of the 500-55-Z chip. Looking at the resonance frequency a comparison was made with respect to the eigenfrequencies obtained from the simulation. It could be observed that the simulated eigenfrequency are representative of the experimental resonance frequency obtained from the mechanical characterization. The variability between the simulated and the experimental frequencies is around 30 KHz, which is less than 4%. With this in mind, it can be concluded that there is a fairly good correlation between the simulation and the experimental results.

Looking at the resonance frequency perspective a comparison was made with respect to the eigenfrequencies that we obtained from the simulation and the details are shown in [Table 5.2](#). It could be observed that the simulation's eigen frequency was not exactly that of the resonance frequency but however there was a variability of only 30 KHz which is less than 4%. With this in mind it can be concluded that there is a fairly good correlation between the simulation and the experimental results.

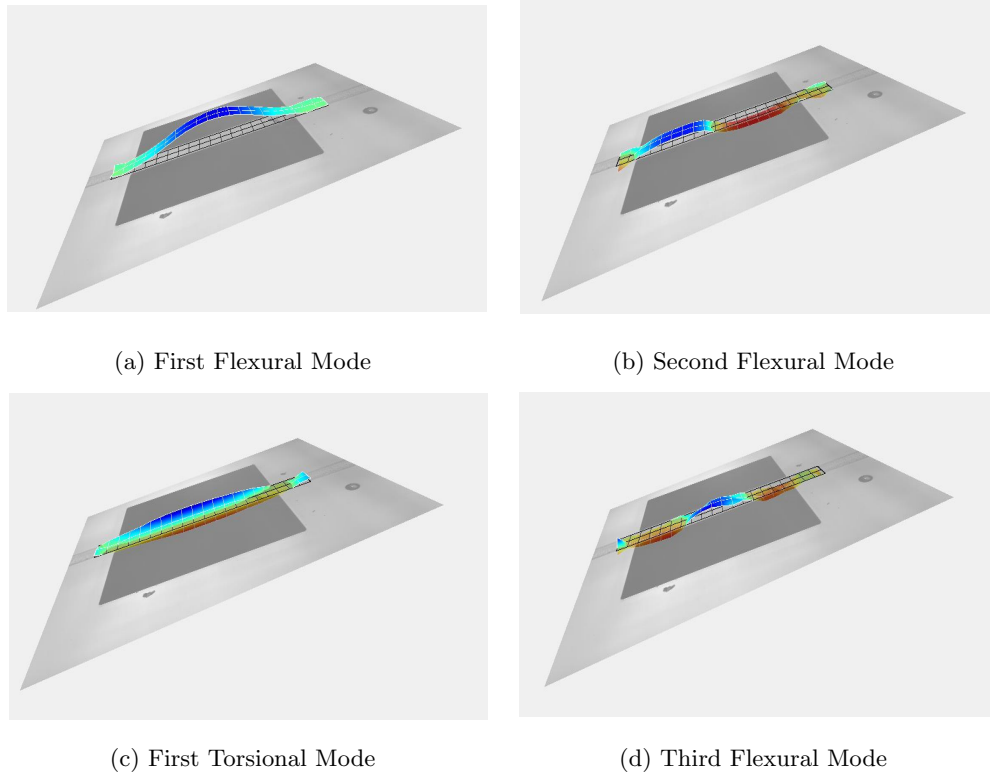


Figure 5.4: A figure illustrating the mechanical modes of the 500-55-Z in air experimentally.

	Resonance Frequency [MHz]	Eigen Frequency [MHz]	Percentage Change %
First Flexural Mode	1.004163	1.0334	2.91
Second Flexural Mode	2.623035	2.6415	0.70
First Torsional Mode	3.081982	2.9791	3.34
Third Flexural Mode	4.494788	4.6043	2.44

Table 5.2: A table illustrating the summary of the experimental frequencies and eigenfrequencies associated with different modes of the 500-55-Z microchannel resonator.

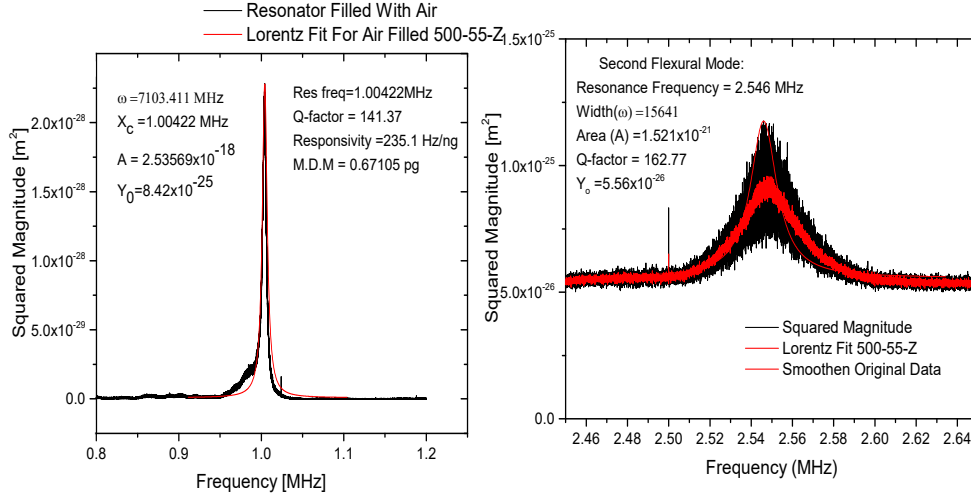
The main reason why there is a difference in frequency is mainly due to the difference between the computed mass (in the simulation design) and the real mass of the resonator. In fact, the fabrication process is known to be a source of variability, due to the tolerance between nominal dimension settled for the SMR design and the dimension obtained from the fabrication. The difference among the designed and the real dimensions can be in the range of 1 to 5 μm . This is affected both by the alignment procedure of the laser and by the KOH etching process. This means that there is an uncertainty pertaining to the uniformity associated with the rectangular shape of the channel across the length of the suspended microchannel resonator. This uncertainty accumulates in terms of mass explaining the reason why the experimental resonance frequency is slightly smaller than the simulated eigenfrequency.

Where Y_o is representing the minimum squared magnitude. X_c is the resonance frequency and w is the full width half maximum of the t and finally the A is the area. The two important parameters needed in order to compute the quality factor were the resonance frequency and the width at 3dB. The q -factors associated to each resonance mode are reported in Figure 1.4. Furthermore, the Vibrometer software allows to obtain from the grid scan analysis the visual reconstruction of the modes shape, reported in Figure 5.4. In principle, the quality factor that could be obtained using the vibrometer's presentation software was really bad in fitting the resonance frequency. The only way by which the quality factor can be obtained is by saving the data in txt format. This would thereafter be processed using the origin software. The origin software provided the opportunity to fit the resonance frequency with a Lorentzian function which is expressed in Equation 5.2 below.

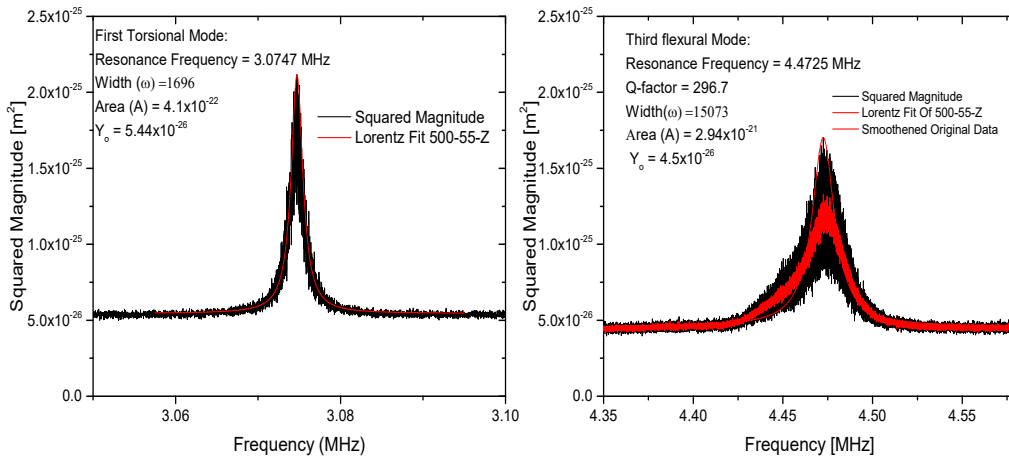
$$Y = Y_o + \frac{2A}{\pi} \left[\frac{w^2}{4(X - X_c)^2 + w^2} \right] \quad (5.2)$$

Where Y_0 is representing the minimum squared magnitude. X_c is the resonance frequency and w is the full width half maximum of the fit and finally the A is the area. The two important parameters needed in order to compute the quality factor were the resonance frequency and the full width half maximum defined at 3dB bandwidth as shown in Equation 5.3. The associated q-factor of the first mode is shown in Figure 5.5a while the second mode had a quality factor of Figure 5.5b. The quality factor of the first torsional mode is shown in Figure 5.5c with the final mode of third flexural mode shown in Figure 5.5d

$$Q - factor = \left[\frac{X_c}{\omega} \right] \quad (5.3)$$



(a) Lorentz Fit For The First Flexural Mode (b) Lorentz Fit For The Second Flexural Mode



(c) Lorentz Fit For The First Torsional Mode (d) Lorentz Fit For The Third Flexural Mode

Figure 5.5: A figure illustrating the Lorentzian fit of the 500-55-Z in air experimentally.

5.2.1 Frequency stability analysis: Allan's Deviation

The Allan's deviation is an important parameter that is mostly used by the scientific community to evaluate the frequency stability of electro-mechanical devices. The Allan's deviation is defined as the square root of Allan's variance. From the experimental point of view. The Allan's deviation relative to the glass SMR has been obtained performing first a sweep measurement to identify the resonance frequency and the related phase inversion Figure 5.6. Having obtained the slope and the intercept these two were inserted into matlab code which implementing the the expression Equation 5.4 and Equation 5.5.

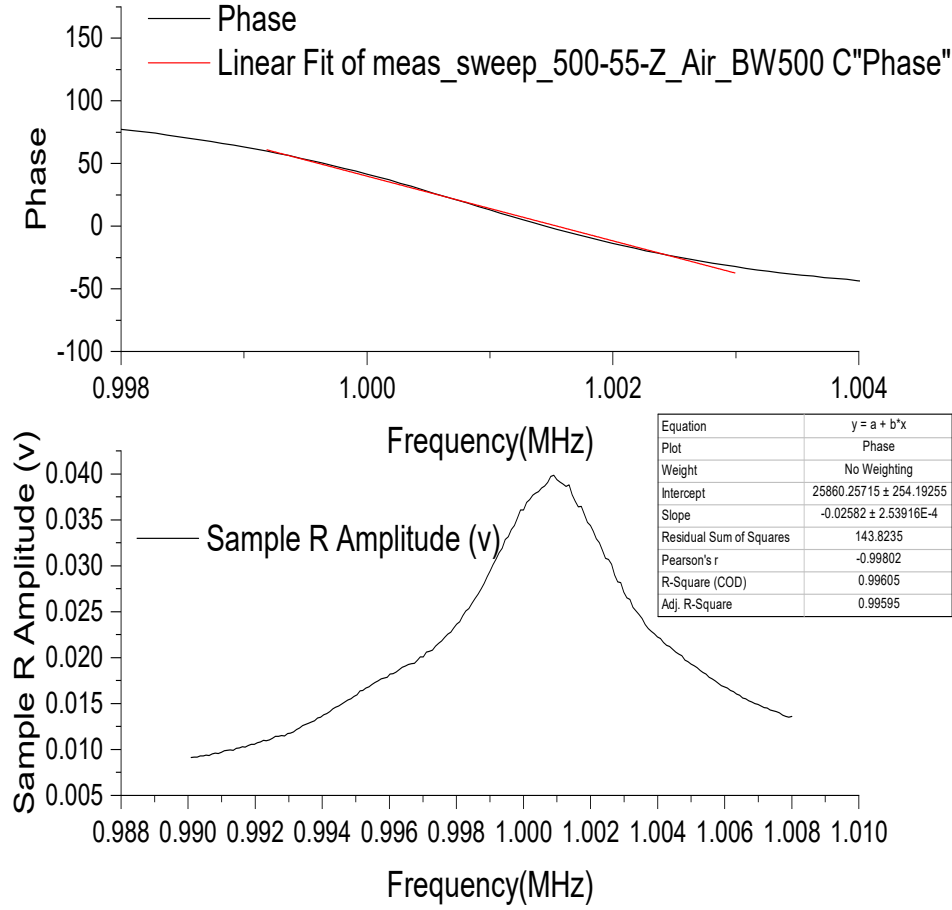


Figure 5.6: A figure illustrating the open loop technique.

$$\sigma_y^2(\tau) = \frac{1}{2} * \langle (\Delta_y)^2 \rangle, \quad (5.4)$$

$$\sigma_y^2(\tau) = \frac{1}{2(N+1)} \left[\sum_{i=1}^N (Y_{i+1,\tau} - Y_{i,\tau})^2 \right].$$

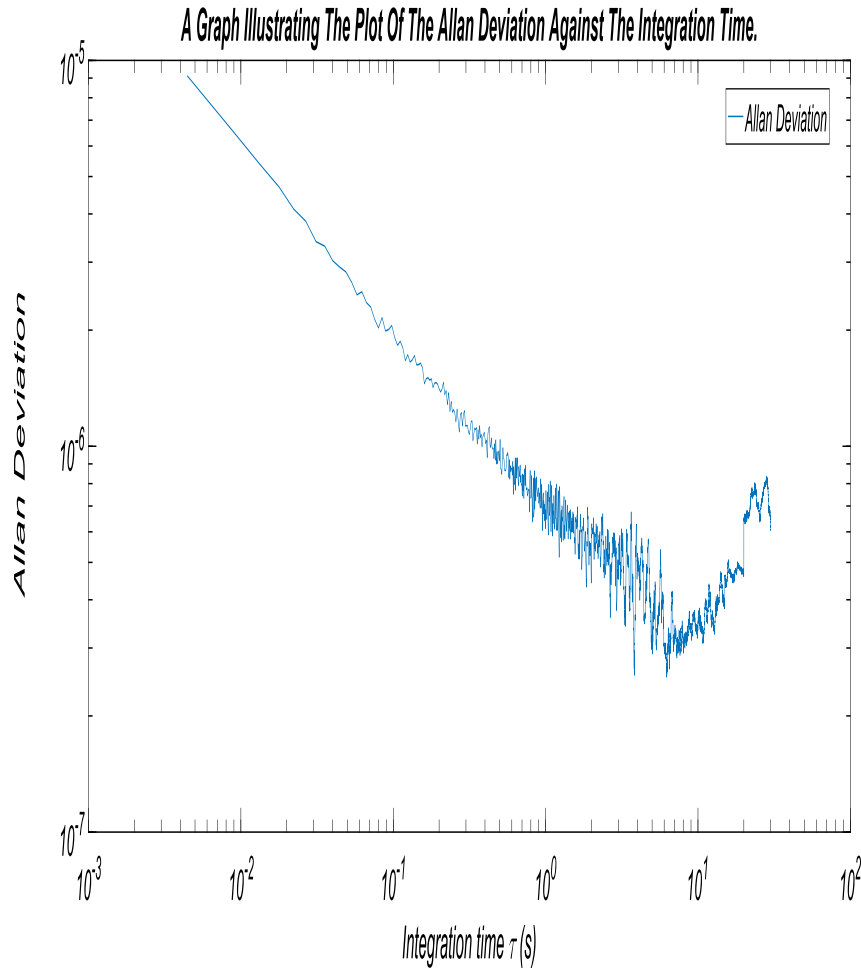
It can be understood that the Y_i is given by:

$$Y_{i,\tau} = \frac{1}{\tau} \int_{i-1,\tau}^{i,\tau} Y(t) dt \quad (5.5)$$

This helped them to obtain the as shown in Equation 5.6. The minimum point associated with the micro resonator is given by Equation 5.6. The real allan deviation is as shown in Figure 5.7 applying a bandwidth of 500Hz. This bandwidth is defined as the difference between the upper and the lower cut-off frequency for the bandpass filter.

$$\frac{\Delta F}{F} = 2.3 * 10^{-7}. \quad (5.6)$$

The minimum as illustrated in the Figure 5.7 which is given in Equation 5.6 is extremely important in the sense that it will enable us to compute the minimum detectable mass according to the expression



.pdf

Figure 5.7: A figure illustrating the allan deviation associated with the 500-55-Z micro resonator.

Equation 5.7.

$$\frac{\Delta F}{F} = \frac{\Delta m}{2 * m},$$

$$\frac{\Delta F}{F} = 2.3 \times 10^{-7}. \quad (5.7)$$

$$\Delta m = 2 * (m) * 2.3 \times 10^{-7}.$$

5.3 Measurement of liquids with different density

After the mechanical characterization, each suspended microchannel resonators have been tested as effective sensor of density. In order to operate with liquid a PDMS microfluidic interface have been bounded to the microchannel resonator chip as explained in [chapter 3](#). The resonator was set up shown in [Figure 5.8](#) so that we can pump the liquid through the micro channel resonator.

In this [section 5.3](#) will be discussed in detail the results obtain from the liquids characterization performed with the 500-55-Z microchannel resonator. In the next [chapter 6](#) will resume and compare all the suspended microchannel resonator devices. The liquids characterized were that were the same used in the simulations approach and are: citric acid (25 % water solution), water and ethanol. It must be emphasized that the corresponding resonance frequencies in the fluid measurement was performed using the only the first flexural mode. In fact, as observed from the mechanical characterization this was the mode showing the best signal to noise ratio, thanks to the highest amplitude of vibration if compared to the others modes. The 500-55-Z micro resonator was filled with fluids and mechanically characterized using the vibrometer. The liquids that were used are the citric acid, water and ethanol as

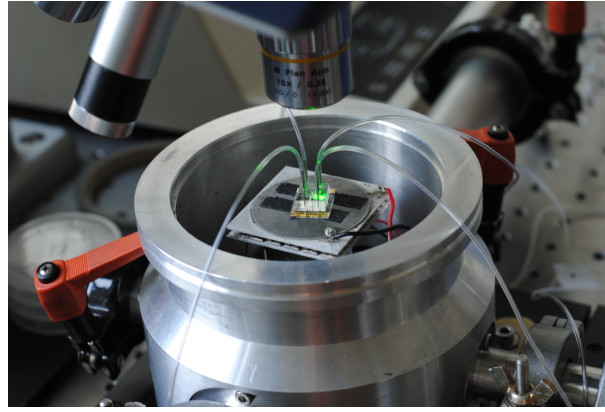


Figure 5.8: A figure illustrating the set up for the liquid measurement

shown in Figure 5.10a. It must be emphasized that the corresponding resonance frequencies in the fluid measurement was performed using the only the first flexural modes. This was because the first flexural mode had the highest amplitude making the shift clearly visible.

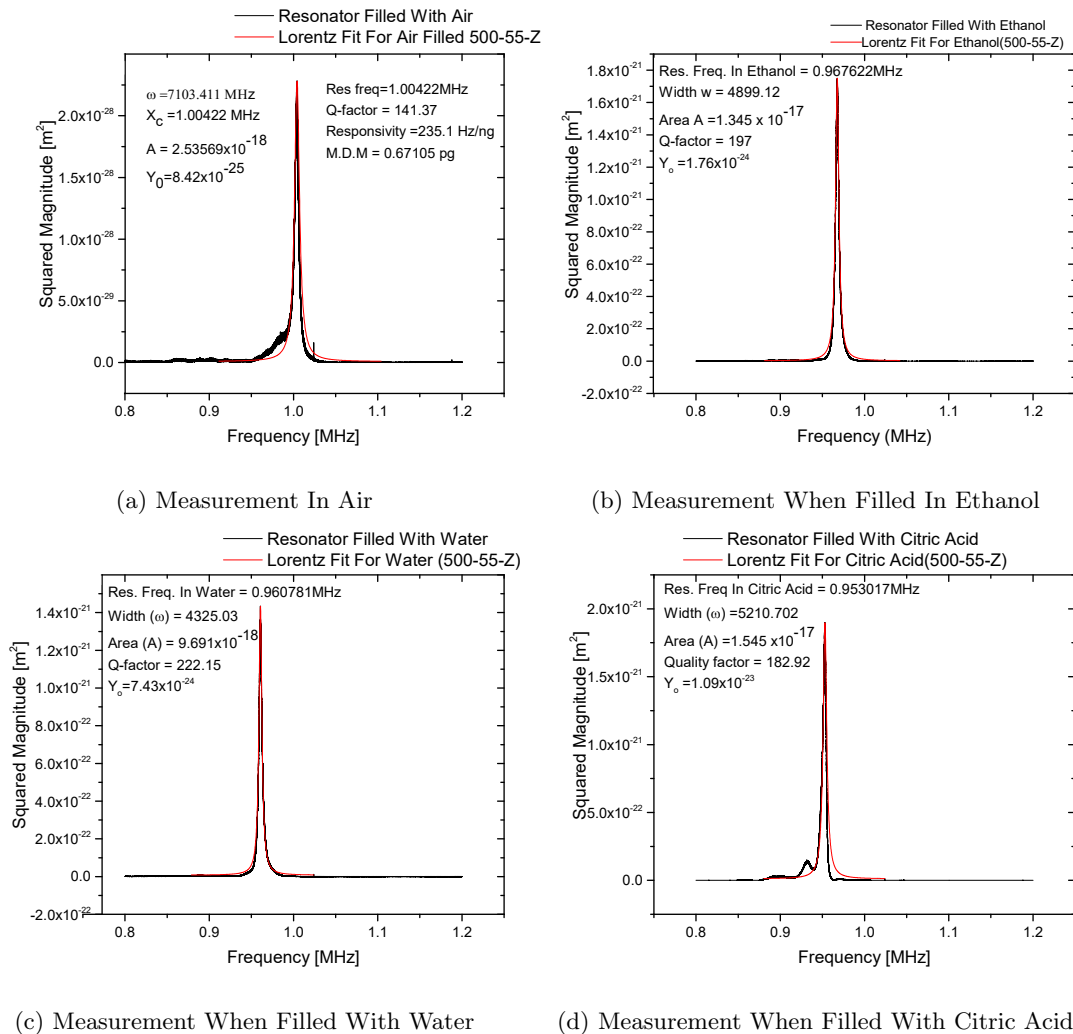
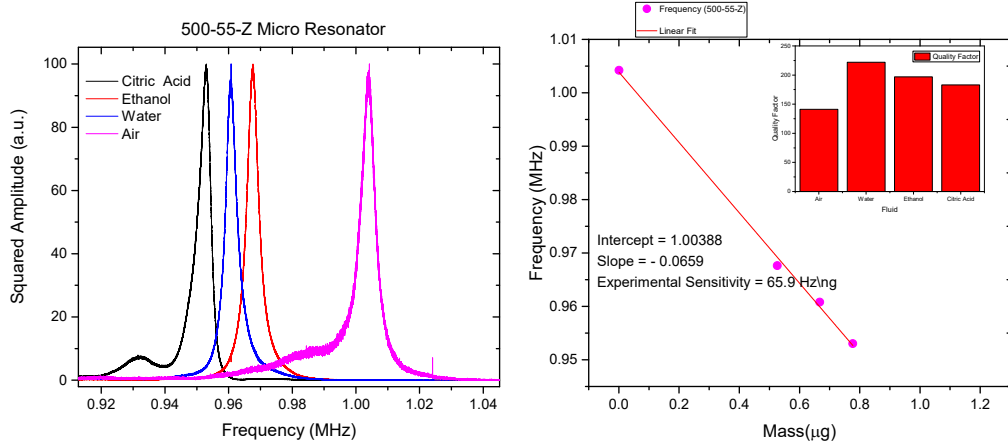


Figure 5.9: A figure illustrating the 500-55-Z micro resonator measurement filled with fluids.

It could be seen explicitly that when the micro resonator was filled with air the resonance frequency was around 1.00422 MHz as shown in Figure 5.9a. The same micro resonator was filled with ethanol and the corresponding resonance frequency shifted to the left to a value of 0.967622 MHz as shown in Figure 5.9b. The main reason why it shifted to a lower values was because of the additional mass of the fluid which increase the effective mass. The same resonator was then filled with water which is known to



(a) A figure illustrating the combinational plot of the 500-55-Z resonator when filled with different fluids (b) A figure illustrating the calibration plot of the 500-55-Z resonator filled with different fluids

Figure 5.10: A figure illustrating the experimental results.

be much denser than ethanol shifting the resonance frequency to a lower value of 0.960781MHz as shown in Figure 5.9c. Finally the same resonator was filled with citric acid which was far denser than water resulting in a resonance frequency of 0.953017MHz as shown in Figure 5.9d.

The fluids measurements are normalized and combined as shown in Figure 5.10a. It is observed that by filling the micro resonator with the liquids the resonance frequency shifted to lower values. This is because of the increase of the effective mass. The citric acid shifted most followed by water and ethanol. This is in complete agreement with their densities since citric acid is the most dense, followed by water and ethanol. Finally the Figure 5.10b is a calibration plot aimed at obtaining the experimental mass sensitivity of the micro resonator which is shown to be around 65 Hz/ng. It could be seen that the experimental responsivity with the fluid was almost a quarter of the mass sensitivity. Even though it is known that the theoretical responsivity and experimental responsivity should maintain their slope. This is because the micro resonator is always the same the only difference is the fluid filling the channel.

	Experimental [MHz]	Simulation With Comsol [MHz]	Percentage Change %
Results In Air	1.00422	1.0334	-
Results With Ethanol	0.967622	0.9507	3.64
Results With Water	0.960781	0.94645	4.32
Results With Citric Acid	0.953017	0.93386	5.1

Table 5.3: An table illustrating the summary of the results for the 500-55-Z

5.4 Evaluation of the SMRs performance and comparison with the simulation data

5.4.1 Simulation Micro Resonator

The simulation of the remaining three micro channel resonators was performed in the same way as explained in this subsection 5.4.1. It must be emphasized that the simulation was done to obtain a rough idea of the eigenfrequency so that we can be able to narrow our characterization. In Table 5.4 are resumed the resonance frequencies for different modes and for different filling liquids. The first torsional mode together with the first, second and third flexural mode are all located within the bandwidth of 0.5MHz to 5MHz for the 500 μm long resonator. The 750 μm long microchannel resonator on the other hand is known have the first torsional together with the first, second and third flexural mode all located within the bandwidth of 0.3MHz to 2.5MHz. It have also been revealed from our previous discussion that by increasing the length of the resonator it means that the mass is correspondingly increased, and the eigenfrequency is shifted to the lower values as shown in the Table 5.4.

	500-55-Z	500-55-Z0	750-30-XX	500-55-X
First Flexural Mode	1.0334	1.0336	0.4938	1.0905
Second Flexural Mode	2.6415	2.625	1.3341	2.7688
First Torsional Mode	2.9791	2.9895	1.9448	2.9567
Third Flexural Mode	4.6043	4.6456	2.4709	4.534
Eigen.F. Ethanol	0.9507	0.95105	0.4693	0.97318
Eigen.F. Water	0.94645	0.94677	0.46516	0.96361
Eigen.F. Citric Acid	0.93386	0.9342	0.46145	0.94747

Table 5.4: A table illustrating the summary of the eigen frequency associated with the different micro resonator.

Accordingly to the experimental conditions used for the 500-55-Z characterization, the fluid simulations were performed by monitoring the fundamental mode. The microchannel resonators was filled with ethanol, water and citric acid (25%). The results of the simulation as shown in Table 5.4. This reveals that most dense liquid which is the citric acid shifted the fundamental eigenfrequency the most and was followed by water and the least shift was encountered in ethanol. This trend was repeated in all the resonator simulation with liquids.

5.4.2 Experimental Results

The results obtained from the simulation were compared with the experimental data deriving from the mechanical characterization of each suspended microchannel resonator. Furthermore, for the different geometries was computed the responsivity taking into account the frequency of the first flexural mode and the mass of each resonator. This parameter and the frequency stability (Allans deviation) were compared with the data obtained from the suspended microchannel resonators without constriction. This was made in order to evaluate how the presence of the constriction can affect the mechanical properties of the resonator. Finally, the performance of the suspended microchannel resonator were validated testing liquids with different density and computing the experimental sensitivity. As it is possible to observe from the Table 5.5, the fundamental parameters (Quality factor, Allan's deviation and responsivity) linked to the mechanical behavior of the resonator are homogeneous among the suspended microchannel resonator (with constriction) that has the same beam length.

The quality factor among the microchannel resonator (with constriction) was found to be highest in 500-55-X which is 288.84. The major way by which the energy is lost can be the medium, the clamping and the constrictions. As it is possible to observe from the Table 5.5, for the suspended microchannel resonator with the constriction the Q does not change in a significant way from the air to the vacuum environment. If we compare the Q values of the suspended microchannel resonator with same geometries but with and without constriction, we can observe a reduction of this parameter and we can probably assume some effects of the constriction presence. Nevertheless, the frequency stability seems to be unaffected by this element. This is further confirm by the results obtained from the computation of the responsivity for the SMRs with and without constrictions. For the 500 um long beam, the computed responsivity seems to be comparable with the one computed for the same length beam with constriction. For the 750 um long beam it has been observed the same behavior between the results obtained from the two type of

	500-55-Z	500-55-Z0	750-30-XX	500-55-X	500-55	750-30
Frequency In Air[MHz]	1.00416	1.00108	0.46300	1.01200	0.8289	0.4585
Frequency In Ethanol	0.967622	0.959360	0.442863	0.97686		
Frequency In Water	0.960781	0.949623	0.438842	0.969282		
Frequency In Citric Acid	0.953017	0.942685	0.435424	0.961948		
Quality Factor In Air	141.37	283.77	110.31	288.84	612	250.43
Quality Factor In Vacuum	329.38	283.77	164.44	295.24		
Mass of Resonator[μg]	2.130	2.13140	4.562	1.987	1.27	2.60
Allan Deviation [ppm]	0.25	0.23	0.38	0.15	1.64	0.30
Responsivity[$\frac{Hz}{ng}$]	235.1	340.8	50.8	254.8	239	120
Experimental Sensitivity	65.9	70.53	36.0	54.68		
Minimum Detectable Mass[pg]	0.67105	0.6756	3.650	0.3234	-	1.15

Table 5.5: A table illustrating the summary of the mechanical characterization associated with the different micro resonator.

(with and without constriction). On the contrary, comparing this responsivity the one associated to the 500 μm long beam, it is possible to observe a reduction of one order of magnitude of this parameter. In this case the major phenomena that affect the results obtained are the increase of the resonator mass and the reduction of the resonance frequency for the 750 long beam. The theoretical sensitivity or the mass sensitivity actually denotes the maximum possible sensitivity that can be achieved. The highest theoretical sensitivity was found in the resonator in the 500 length micro resonator because it had the lower mass with respect to the 750 micro resonator as illustrated in the [Equation 5.8](#). The resonance frequency of the first flexural mode were very similar for all the 500 micro channel resonator.

$$Responsivity = \frac{F_{res}}{2 * Mass} \quad (5.8)$$

The experimental sensitivity was performed for all the micro channel resonator by filling them with the three liquids which are ethanol, water and citric acid. The highest experimental sensitivity was found 500-55-Z0 followed by the 500-55-Z and then the 500-55-X. This seems to suggest that the shape of the internal constriction plays a significant role in improving the experimental sensitivity. This is an additional information that the experimental sensitivity is providing. The experimental sensitivity is found to be about quarter of the theoretical sensitivity (Responsivity). The 750-30-XX micro resonator provided the lowest experimental sensitivity of $36.0 \frac{Hz}{ng}$. The minimum detectable mass was found for the micro resonators always been in the picogram. The smallest value associated with the minimum detectable mass was found to be around 0.3234 pg as shown [Table 5.5](#). For what concern the frequency stability, for both the resonator type the Allan's deviation shows values comprise between 0.15 and 0.38 ppm. The relationship between frequency shift and density of the fluid, filling the suspended microchannel resonator, was the same observed for all the resonators tested, both from the simulation perspective [Table 5.5](#) and from the experimental measurements.

Chapter 6

Conclusion And Recommendation

6.1 Conclusion

This difference in mass resulted in the difference in frequency between the suspended micro-resonator experimental values and the simulated result. Lower values of frequency was encountered using the 750 m length resonator while the 500 m resonator had a frequency around 1 MHz in air. This is a strong evidence that the resonance frequency for a micro channel resonator have a inverse dependence on the effective mass [3].

The SMRs are recently attract great attention in the field of the biosensing, and in particular in the density and mass monitoring of cells, bacteria growth and particles loading. In this work, it has been proposed a new SMRs design, characterized by the presence of specific obstacles that in principles, could be used to reduce the liquid flow velocity in the middle of the suspended beam. This means to have the possibility to increase the time of permanence in that beam region, which gives the higher amplitude signal. The main purpose of this thesis work was to understand how the mechanical behavior of SMRs could be affected by the presence of this constriction geometries build inside the hollow channel. In order to do that the work was organized in two step: first the simulation of the mechanical behavior of the SMRs with and without liquids inside; and second the experimental confirm of this behavior. Furthermore, the mechanical performance of the SMRs containing the constriction have been compared with SMRs characterized by the same dimensions but without constriction. Generally, it could be concluded that the simulation of the eigenfrequency of the suspended microchannel resonator, even though some little difference, are consistent with the experimental evidence. The small variability can be mainly justify taking into account the variability of the fabrication techniques (femtosecond laser irradiation followed by the chemical etching). In fact, we saw from the SEM analysis variation of about 5 um between the nominal dimensions and the one obtained after the fabrication.

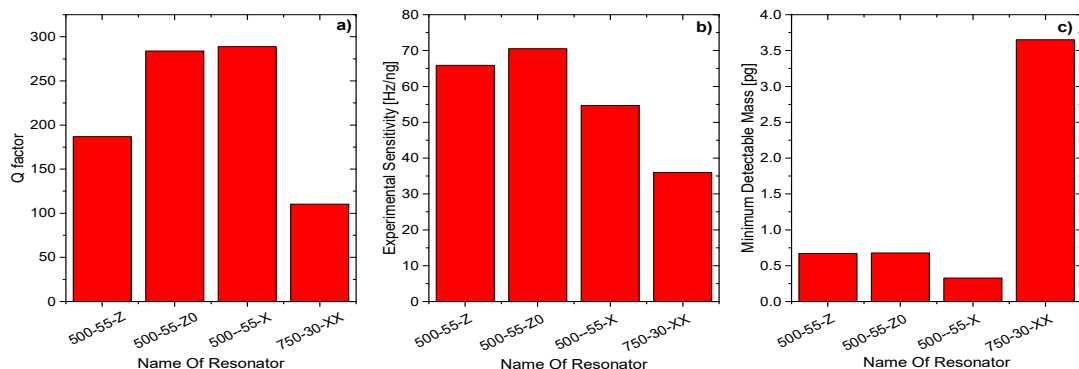


Figure 6.1: A figure illustrating the performance of the different resonators using experimental sensitivity and the quality factor.

The best performing resonator has been determined by the comparative analysis of Q factor, experimental sensitivity and minimum detectable mass, which takes into account also the contribution

of the frequency stability analyzed by the means of the Allans deviation analysis. Taking a carefully look at [Figure 6.1](#) one can recognize the 500-55- X as the best resonator. In fact, this SMR provided the minimum detectable mass and the highest quality factor. The 500-55-Z0 microchannel resonator can be also considered as SMR with high mechanical performance, thanks to its high experimental sensitivity and the high quality factor, comparable with the 500-55-X device. Furthermore, from the analysis of the SMRs performance it is possible to settle that the presence of the constriction does not affect in a negative way the mechanical characteristics of the resonators. The Q factor seem to be in part affect by the presence of the constriction, but only a small variation of the responsivity and of the frequency stability have been observed between the two types of SMRs. The as fabricated devices can be used as effective platform for the characterization of liquids with different density, In fact, the performance for this kind of measurement have been tested evaluating the SMR response as function of different filling liquids. From the experimental point of view, parameters like the quality factor did not degraded excessively when the suspended microchannel resonator was filled with the solution, confirming the non-monotonic energy dissipation as function of the fluid viscosity, which is the fundamental characteristic of this platforms.

In the future there will be the need to perform more specific tests to evaluate the impact of the constriction onto the flow velocity and to the ability to slow downparticles and/or cells in the middle region of the burried channel. This study must be done from both the simulation and the experimental point of view. In this thesis only micro channel resonators were considered. There is also the need to consider the extend the concept studied in this thesis to the nanochannel resonator. This will demand a completely different fabrication techniques. It is hereby recommended that there is the need to upgrade the politecnico nanomechanical lab so that it can be used to fabricate more sophisticated nanomechanical resonator. It is also recommended that if the Italian government take immediate steps to acquire the FLICE set-up for easy nano-mechanical experimentation in Italy.

Bibliography

- [1] B. L. Adams, T. Mason, T. Olson, and D. Sam. Theory of Grain Boundary Structure Effects on Mechanical Behaviour. *Materials Science Forum*, 157-162:1731–1738, 1994. ISSN 1662-9752. doi: 10.4028/www.scientific.net/MSF.157-162.1731. URL <http://www.scientific.net/MSF.157-162.1731>.
- [2] B. L. Adams, A. Henrie, B. Henrie, M. Lyon, S. R. Kalidindi, and H. Garmestani. Microstructure-sensitive design of a compliant beam. *Journal of the Mechanics and Physics of Solids*, 49(8):1639–1663, Aug. 2001.
- [3] B. L. Adams, S. R. Kalidindi, and D. T. Fullwood. *Microstructure Sensitive Design for Performance Optimization*. Butterworth-Heinemann, Waltham, MA, 2013.
- [4] K. Aicher. Multiphoton ionization of molecules: A comparison between femtosecond and nanosecond laser pulse ionization efficient. *Science Direct*, 6:1059–1068, Nov. 1995. doi: 10.1016/1044-0305(95)00551.
- [5] L. Aigouy. Near field scattered by a single nanoslit in a metal film. *Applied Optics*, 46, Dec. 2007. doi: 10.1364/AO.46.008573.
- [6] J. Blake. Biosensing using dynamic mode cantilever sensors. *Science Direct.*, 32:1–18, Jan. 2012. doi: 10.1016/j.bios.2011.10.054.
- [7] T. P. Burg. Weighing of biomolecules, single cells and single nanoparticles in fluid. *Nature Letters*, 446(9), Apr. 2007. doi: 10.1038/nature05741.
- [8] T. P. Burg and S. Manalis. Vacuum-Packaged Suspended Microchannel Resonant Mass Sensor for Biomolecular Detection. *Journal of microelectromechanical system*, 15(6), Dec. 2006. doi: 10.1109/JMEMS.2006.883568.
- [9] S. Byun. Characterizing the deformability and surface friction of cancer cells. *Proc. Natl. Acad. Science*, 110(19):7580–7585, Mar. 2013.
- [10] J. Chan. Structural changes in fused silica after exposure to focused femtosecond laser pulses. *Optical Society Publishing*, 26:1726–1728, Mar. 2001. doi: 10.1364/OL26.001726.
- [11] J. M. Chris. Morphology of femtosecond laser-induced structural changes in bulk transparent materials. *Appl. Physics Letters*, 84(9), Mar. 2004. doi: 10.1063/1.1650876.
- [12] S. Davis, Miura and Hirao. Writing waveguides in glass with a femtosecond laser. *Optics Letters*, 21:1729–1731, 1996. doi: 10.1364/OL.21.001729.
- [13] L. Donghyuk. Pulled microcapillary tube resonator with electrical readout for mass sensing application. *Scientific Report*, 6:1–8, Oct. 2016.
- [14] D. Du. Laserinduced breakdown by impact ionization in SiO₂ with pulse widths from 7 ns to 150 fs. *Applied Physical Letters*, 64:3070–3071, Nov. 1994. doi: 10.1063/1.111350.
- [15] A. A. Ferri and E. H. Dowell. The behavior of a linear, damped modal system with a non-linear spring-mass—dry friction damper system attached, part 5II6. *Journal of Sound and Vibration*, 101(1):55–74, 1985. URL <http://www.sciencedirect.com/science/article/pii/S0022460X85800389>.
- [16] D. Gattas and M. E. Femtosecond laser micromachining in transparent materials. *Nature Photonics*, 2:219–225, Apr. 2008.

-
- [17] M. Godin. Using buoyant mass to measure the growth of single cell. *National Method*, 7(3):387–390, May 2010.
- [18] M. Grover. Measuring single cell density. *Proc. Nat. Acad. Sci*, 2011.
- [19] T. Itoh and T. Suga. Force sensing microcantilever using sputtered zinc oxide thin film. *App. Phy. Letters*, 64(1), Jan. 1994. doi: 10.1063/1.110913.
- [20] A. Killi and D. Kopf. Optical waveguide writing with a diode-pumped femtosecond oscillator . *Optic Express*, 29(16):1900–1902, 2004. doi: 10.1364/OL.29.001900.
- [21] S. Koji and Dong. Femtosecond laser 3D micromachining: a powerful tool for the fabrication of microfluidic,optofluidic, and electrofluidic devices based on glass. *ResearchGate*, 14(9):3447–3458, 2014. doi: 10.1039/c41c00548.
- [22] P. Langs. Microcantilever Sensors. *Springer-Verlag Berlin heidelberg*, 14(8), Jan. 2007.
- [23] A. Marcinkevicius. Femtosecond laser-assisted three-dimensional microfabrication. *Optical Letters*, 26(5):277–279, 2001.
- [24] S. Olcum. High-speed multiple-mode mass-sensing resolves dynamic nanoscale mass distributions, 2015. URL web.mit.edu/newsoffice/">MITNewsMay12, 2015.
- [25] R. Osellame. Femtosecond laser microstructuring: an enabling tool for optofluidic lab-on chip. *Laser and photonics reviews*, 3:442–463, 2011.
- [26] T. R.C. Ultra-high resolution index of refraction profiles of femtosecond laser modified silica structures . *Optic Express*, 11(3):775–781, 2003. doi: 10.1364/OE.11.000775.
- [27] R. Taylor. Applications of femtosecond laser induced nanocracks inside fused silica glass. *Laser Photonic Review*, 2:26–48, Nov. 2008.
- [28] P. B. Thomas and R. M. Scott. Weighing of biomolecules, single cells and single nanoparticle in fluid. *nature*, 446(5741):484, 2007.
- [29] T. Thundat. Detection of mercury vapour using resonating microcantilevers. *Appl. Phys.*, 66(66): 1695–1697, 1995.
- [30] S. Timoschenko. *Vibration Problem In Engineering*. D. Van Nostrand Company Inc., 1937.
- [31] J. Tomayo. Biosensors based on nanomechanical system. *Chem. Society Review*, 42(3), Mar. 2013.
- [32] E. Ventsel. Thin plates and shell:Theory,Analysis and Application. *Marcel Dekker Newyoke*, 4(3), Dec. 2001.
- [33] E. Verpoorte. Beads and chips : new recipe for analysis. *Scientific Report*, 7:13–28, Nov. 2003. doi: 10.1039/b31327j.
- [34] L. G. Villanueva. *Fundamentals Of Nanomechanical Resonators*. Springer Nature, 2016. ISBN 978-3-319-28689-4. doi: 10.1007/978-3-319-28691-4.
- [35] J. Wilbur and J. W. Chan. Spectroscopic characterization of different femtosecond laser modification regimes in fused silica. *OSA Publishing*, 24(7):1627–1632, 2007.
- [36] R. Wilfinger. The Resonistor:A frequency selective device utilizing the mechanical resonance of silicon substrate. *IBM. Journal Res. Dev.*, 12(11):113–118, Jan. 1968.

List of Figures

1.1	Operation scheme of a cantilever sensor based on static mode detection. A DNA hybridization is shown in the above experiment: The sensor's output is the cantilever deflection. [31].	14
1.2	Operation scheme of cantilever based on dynamic operational mode. Mass variations of the oscillator are related to the resonance characteristic of the structure.	14
1.3	A figure illustrating the dynamic-mode cantilevers	15
1.4	Representation of the two operational modes of SMR A. The SMR translates the mass charge into changes of frequency whiles the fluid continuously flow through the channel B. Is a surface adsorption mechanism in which the molecules binds to the channel. C. The particle that flow the SMR without binding to the surface can be observed depending on their position in the channel. [7]	16
1.5	Representation of the two SMR having different fluids that used in the Groove's article [18]	17
1.6	A figure illustrating a classical HNR that was used as electrophoresis assisted time of flow mass spectrometry.	18
1.7	The fabrication and packaging process of a suspended microchannel resonator [8].	19
1.8	The fabrication of a microcapillary tube resonator [13].	20
2.1	This figure illustrate the beam. [34]	23
2.2	A figure illustrating the plot of the roots associated with the frequency equation shown in Equation 2.27	26
2.3	A figure illustrating the first four bending modes of the double clamped beams.	26
2.4	A figure illustrating the damped one dimensional oscillator with one degree of freedom [34].	27
2.5	A figure illustrating Equation 2.44 the $z_o=1, \Omega=1$ and $\zeta=0.03$ from [34].	29
2.6	Driven damped vibration of a lumped system schematic drawing of a resonator A . Driven by force Equation 2.52 D . Driven by an external vibration. B . and E . show the respective relative amplitude response [34].	30
2.7	Quality factor extracted from the amplitude frequency spectrum of a mechanical resonator [7].	31
2.8	A quality factor plotted against the number of mode of a cantilever [34].	31
2.9	Eigenfrequency Ω of linear resonator as a function of arbitrary input parameter ε . The red line represents the slope at ε_o which is the responsivity \mathfrak{R} . [34].	32
2.10	The different noise regime of the allan deviation [34].	33
3.1	The femtosecond laser microstructuring applied in the fabrication of waveguide. With the refractive index contrast between the waveguide and the pristine glass is about $\Delta n = 1.0 \times 10^{-3}$ [25].	35
3.2	A figure illustrating multiphoton scattering, tunneling ionization and the avalanche ionization	36
3.3	A figure illustrating setup of the femtosecond laser writing from [25] article.	39
3.4	A figure illustrating the FLICE technique which was optimized in collaboration with the FEMTOprint [®]	40
3.5	A figure illustrating the images and the schematics associated with different constriction of the suspended micro channel resonators.	41
3.6	A figure showing the SEM image for A. $55\mu\text{m}$ B. $30\mu\text{m}$ channel micro-channel resonator	42
3.7	A figure showing the silicon mold process A . Deposition of the negative photoresist B . Exposure C . Development D . Dry Etching E . Stripping F . Passivation with PFOT G . PDMS deposition H . PDMS Mold	42
3.8	A figure showing the final product after the bonding	43
4.1	A figure showing the electronic unit of the polytec laser scanning vibrometer	47
4.2	A figure showing the scanning vibrometer of the polytec laser scanning vibrometer	48

4.3	A figure showing the polytech scanning vibrometer operation.	48
4.4	A figure showing the loading of the micro channel resonator	49
4.5	A figure showing the loading of the micro channel resonator with the micro tubes for the liquids measurement.	50
5.1	A figure illustrating the meshing and the fixed domain 1 and 5 of the 500-55-Z micro resonator.	51
5.2	A figure illustrating the shape of the constriction of the 500-55-Z Micro Resonator	52
5.3	A figure illustrating the simulated modes of the 500-55-Z in Air.	52
5.4	A figure illustrating the mechanical modes of the 500-55-Z in air experimentally.	54
5.5	A figure illustrating the lorentzian fit of the 500-55-Z in air experimentally.	55
5.6	A figure illustrating the open loop technique.	56
5.7	A figure illustrating the allan deviation associated with the 500-55-Z micro resonator.	57
5.8	A figure illustrating the set up for the liquid measurement	58
5.9	A figure illustrating the 500-55-Z micro resonator measurement filled with fluids.	58
5.10	A figure illustrating the experimental results.	59
6.1	A figure illustrating the performance of the different resonators using experimental sensitivity and the quality factor.	63

List of Tables

- 2.1 An table illustrating the potential and kinetic energies of a double clamped beam 22
- 3.1 A table illustrating the summary of the geometrical characteristics associated with the different micro resonator. 40
- 4.1 A table illustrating the eigen frequency when the 500-55-Z micro resonator was filled liquids using comsol simulation. 46
- 5.1 A table illustrating the eigen frequency when the 500-55-Z micro resonator was filled liquids using comsol simulation. 53
- 5.2 A table illustrating the summary of the experimental frequencies and eigenfrequencies associated with different modes of the 500-55-Z microchannel resonator. 54
- 5.3 An table illustrating the summary of the results for the 500-55-Z 59
- 5.4 A table illustrating the summary of the eigen frequency associated with the different micro resonator. 60
- 5.5 A table illustrating the summary of the mechanical characterization associated with the different micro resonator. 61